Analysis of Electrical Breakdown Influenced by the Statistics of Orthogonal Frequency Division Multiplexing (OFDM) Signals

Chamnap Phok

A thesis submitted for the degree of Master of Engineering Science at
Monash University in 2018

Department of Electrical and Computer Systems Engineering

Copyright notice

© Chamnap Phok (2018).

I certify that I have made all reasonable efforts to secure copyright permissions for third-party content included in this thesis and have not knowingly added copyright content to my work without the owner's permission.

Abstract

Orthogonal frequency division multiplexing (OFDM) is a modulation method used in many broadcasting services, including the European digital video broadcasting-terrestrial (DVB-T) standard. It is an effective solution to intersymbol interference caused by a dispersive channel. At the output of high-power DVB-T transmitters, bandpass-filters are typically used to remove intermodulation products to avoid interferences between the adjacent channels. Electrical breakdown in the form of arcing limits the power handling capability of these filters. Breakdown interrupts the signal transmission and can cause damage to the transmission equipment. This problem has been a concern to broadcasters and filter manufacturers as it is not well understood. A major drawback of OFDM is its high peak-to-average power ratio (PAPR) which plays an important role in causing electrical breakdown. The issue of electrical breakdown caused by OFDM signals has not been previously studied extensively. This project was motivated by unexplained results of breakdown tests of high power filters produced by an Australian manufacturer. By applying findings from fundamental plasma physics to predict the build-up of plasma caused typical DVB-T signals, it is shown how these experimental results can be explained.

Electrical breakdown occurs when the electron density is high enough to create a conductive path between the electrodes. As such, the relationship between the electron density and the time-varying electric field caused by OFDM signals needs to be investigated. A simple approach based on the ionization kinetics equation is used to calculate the instantaneous density of free electrons in a fixed volume of air. The equation is applied to bursts of sinusoidal signals and it is shown that whether breakdown occurs depends on the power and duration of the burst. These results predict that breakdown depends on the short term statistics of the DVB-T signal. Simulation results for the statistical properties of DVB-T signals are presented which show that there is a very strong relationship between the power and the width of peaks in the signal. It is shown that these two findings can be combined to explain the previously unexplained results of the high power filter breakdown experiments.

Possible new types of digital signal processing algorithms are suggested which modify the transmitted signal so that peaks that will cause breakdown are removed.

Declaration of Authorship

This thesis contains no material which has been accepted for the award of any other degree or diploma at any university or equivalent institution and that, to the best of my knowledge and belief, this thesis contains no material previously published or written by another person, except where due reference is made in the text of the thesis.

Signature: 

Print Name: Chamnap Phok

Date: 03/01/2019

List of Publications

Conference Paper

1. C. Phok, A. Neild, D. Pelz, and J. Armstrong, "Analysis on electrical breakdown in OFDM systems," in *2018 Australian Microwave Symposium (AMS)*, 2018, pp. 71-72.

Journal Paper Draft

1. C. Phok, A. Neild, D. Pelz, and J. Armstrong, "The Effect of Peak-to-Average Power Ratio of OFDM in Electrical Breakdown," To be submitted to IEEE Transactions on Broadcasting

Acknowledgements

First of all, I am thankful for the opportunity to be in this postgraduate program. It has been a great place for me to develop myself academically. I would like to express my sincere gratitude to my supervisors, Professor Jean Armstrong and Professor Adrian Neild, for guiding me throughout this journey. A special thanks to Dieter Pelz who made this journey happen and always offered as much help as possible even after retirement. I would like to thank all of my colleagues, Cuiwei He, Kelly Kelly, Mohammed M. A. Mohammed, Stefanie Cincotta and Ye Feng, for providing me with insightful discussions throughout the program. I also would like to thank Lilian Khaw for various consultations on improving my written communication. I have gained so much knowledge from these amazing people.

I would like to also thank the Plasma Theory and Simulation Group (PTSG) who make their OOPD1 code freely available online. OOPD1 code has been very beneficial for this thesis.

All of this would not be possible if it were not for my family who were always there to support me during difficult times. I would like to dedicate this thesis to my beloved parents who make sacrifices to give me a better life.

Contents

List of Figures

List of Abbreviations

AWGN	Additive White Gaussian Noise
BER	Bit-Error-Rate
CCDF	Complementary Cumulative Distribution Function
CLAPR	Calculation-level-to-average power ratio
CR	Clip Ratio
CW	Continuous Wave
DC	Direct Current
DTV	Digital Television
DVB-T	Digital Video Broadcasting-Terrestrial
FFT	Fast Fourier Transform
HPA	High-Power Amplifier
IFFT	Inverse Fast Fourier Transform
ISI	Intersymbol Interference
OFDM	Orthogonal Frequency Division Multiplexing
OOB	Out-Of-Band
OOPD1	Object-Oriented Plasma Device One
PAPR	Peak-To-Average Power Ratio
PIC	Particle-In-Cell
MCC	Monte Carlo Collisions
PSD	Power Spectral Density
PTSG	Plasma Theory and Simulation Group
QAM	Quadrature Amplitude Modulation
RF	Radio Frequency
TV	Television
VHF	Very-High Frequency
UHF	Ultra-High Frequency

List of Symbols

A_n	Amplitude of n^{th} carrier
B	Bandwidth of the signal
E	Electric field
$E(t)$	Instantaneous electric field
E_b	Energy per bit
E_e	Effective electric field
E_0	Amplitude of electric field
E_{rms}	Breakdown electric field
G	Length of the cyclic prefix
I	Oversampling factor
M	QAM constellation size
N	Number of subcarriers in each OFDM symbol
N_0	Noise power spectral density
N_{e}	Number of electrons
P	Signal power
$P(t)$	Instantaneous power of the signal
P_{b}^{CW}	CW breakdown threshold
P_c	Collision probability
P_0	Average power of the signal
P_{p}	Peak power of the waveform
$S(t)$	Multicarrier signal
T	Cycle period of the signal frequency
T_s	Symbol period
T_E	Elementary period
X_k	Data to be carried on the k^{th} subcarrier
Δt	Time step
α	Data symbol vector
α_i	First ionization coefficient
β	Mapped symbol vector
γ	Sum of data symbol power
φ	Phase of n^{th} carrier

$\upsilon(t_k)$	Velocity of electron
$\upsilon_d(t)$	Drift velocity of electron
ρ	Charge density
ω	Angular frequency
σ_n^2	Noise variance
$\boldsymbol{X}$	Frequency-domain signal vector at the IFFT input
$\boldsymbol{x}$	Time-domain signal vector at the IFFT output without oversampling
$\boldsymbol{x^I_{over}}$	Time-domain signal vector at the IFFT output with oversampling
b	Data rate
c	Normalization coefficient
d	Gap between two electrodes
$d_{\max}$	Maximum distance that electrons can travel due to the applied electric field
e	Electron charge
f_c	Carrier frequency of the signal
f_n	Carrier frequency of n^{th} carrier
J	Source of free electrons from cosmic rays
m	Electron mass
n	n^{th} carrier
p	Gas pressure
$s(t)$	Real passband signal
t_0	Time for electron avalanche to reach a steady state
t_k	Time of k^{th} time step
v	Net rate of generation of free electrons
v_a	Attachment frequency
v_c	Average collision frequency
v_i	Ionization frequency
v_T	Total collision frequency of the collisions between electrons and neutral gas molecules
$x(t)$	Complex baseband signal
x_{avg}	Average electron position
x_m	m^{th} time-domain sample without oversampling

List of Operations

$\sum_{n=1}^{N}$	Summation of terms from $n = 1$ to N
$\mathrm{Im}(.)$	Imaginary component of a complex value
$\mathrm{Re}(.)$	Real component of a complex value
$\log_a(x)$	Logarithm of x to base a
X^T	Transpose of a vector X
$\frac{dx}{dt}$	Rate of change of x

Chapter 1: Introduction

1.1 Overview

Orthogonal frequency division multiplexing (OFDM) is a modulation method widely used in many broadcasting services, including the European digital video broadcasting-terrestrial (DVB-T) standard [1] for digital television (DTV). It is well known for being an effective solution to intersymbol interference (ISI) caused by a dispersive channel [2]. Fig. 1.1 shows a simplified graphical representation of the OFDM system for DTV. The high-power transmitter generates a DVB-T signal using OFDM modulation. The transmitting antenna broadcasts the signal over air. The broadcasted signal will be received by the receiving antenna. In the transmission system, the signal needs to be filtered before reaching the transmitting antenna. Bandpass-filters [3] are typically used at the output of high-power DVB-T transmitters [4] to remove intermodulation products in the signal to avoid interferences between the adjacent channels. Filter manufacturers conduct a power handling test to measure the power handling capability of these filters. Electrical breakdown in the form of arcing which occurs during the testing indicates the maximum operating power of the filter. Many broadcasters are concerned with this breakdown problem as it can interrupt the broadcasting and can cause damage to the transmission equipment. Therefore, electrical breakdown must be prevented during the normal operation in the transmission system. However, due to limited understanding of the cause of the breakdown, the current solution is to limit the transmitted power to well below the power handling capability of the filter, which may not be effective.

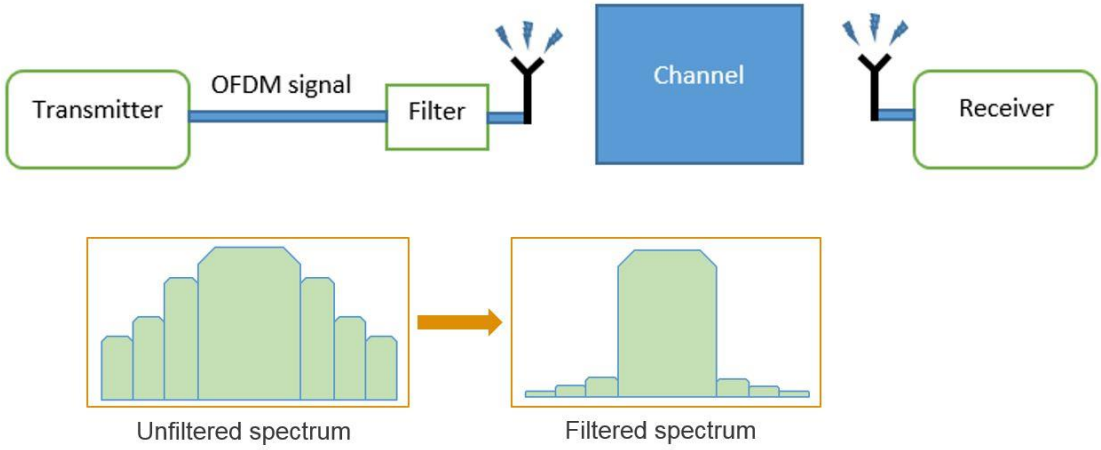

Fig. 1.1. A representation of filtering in an OFDM system for DTV

The problem of breakdown caused by OFDM signals has not been given enough attention and requires much more study if a more effective solution needs to be proposed. A major drawback of OFDM is its high peak-to-average power ratio (PAPR). For example, it is possible for an OFDM signal to have the PAPR of 13 dB. This is equivalent to the peak power being 20 times higher than the average power of the signal. There is a broad range of literature on the problems that the high PAPR of OFDM causes in other situations [5], [6]. For instance, it can limit the average power of the transmitted signal resulting in reduced range of multicarrier transmission. Many techniques have been developed to decrease the PAPR of OFDM [7-14]. There has also been extensive research into electrical breakdown in gases [15-29]. The majority of these studies involve the use of direct current (DC) and continuous wave (CW) signals. However, there is little research on the effect of the PAPR of OFDM on electrical breakdown; thus, it has not been discussed extensively. One of the few studies focuses on the time evolution of electron population caused by multicarrier signals [30]. While this provides a basic understanding of the problem, the analysis is limited to a signal with only a few subcarriers whereas the OFDM signal used in DVB-T signal transmission has either 8192 subcarriers in the 8K mode or 2048 subcarriers in the 2K mode. In addition, breakdown prediction has been conducted based on the statistics of the OFDM signal [31]. However, this prediction does not take into account any particular OFDM signal, so it cannot be used to develop novel signal processing based techniques to mitigate electrical breakdown.

The topic of electrical breakdown can be very broad, so the focus needs to be narrowed down to a specific study to suit the purpose of this research project. Electrical breakdown occurs when the number of free electrons in the air within the filter reaches a critical value creating a conductive path between the electrodes. The occurrence of arcing depends on many factors including the air pressure [32], the geometry of the filter [33], the roughness of inner surfaces [34], and the ionization caused by high-energy electrons. In this research, the relationship between the ionization and the time-varying electric field caused by an OFDM signal is focused upon. This allows the issues related directly to the use of OFDM to be demonstrated without specifying a certain set of filter design parameters.

This project was motivated by unexplained results of breakdown tests of high power filters produced by an Australian manufacturer. The aim of this research is to provide a good understanding of these experimental results by applying findings from fundamental plasma physics to predict the build-up of plasma caused typical DVB-T signals. Theoretical and simulation analyses are used to understand the nature of the problem by investigating the resulting electron density influenced by OFDM signals.

1.2 Contributions of This Research

The effect of OFDM signals on electrical breakdown is studied. A simple approach based on the ionization kinetics equation is used to calculate the instantaneous density of free electrons in a fixed volume of air. The equation is applied to bursts of sinusoidal signals and it is shown that whether breakdown occurs depends on the power and duration of the burst. These results predict that breakdown depends on the short term statistics of the DVB-T signal. Simulation results for the statistical properties of DVB-T signals are presented which show that there is a very strong relationship between the power and the width of peaks in the signal. It is shown that these two findings can be combined to explain the previously unexplained results of the high power filter breakdown experiments. Possible new types of digital signal processing algorithms are suggested which modify the transmitted signal so that peaks that will cause breakdown are removed. The effect of carrier frequency of the signal is investigated and the results show that its effect on electrical breakdown is negligible.

1.3 Outline of the Thesis

This introductory chapter will be followed by the literature review to provide a solid grasp of various research studies previously conducted for this research topic. This will be presented in Chapter 2: Literature Review. Then, the basic OFDM theory will be described in Chapter 3: OFDM Theory. Monte Carlo simulation method and the ionization kinetics equations will be discussed in Chapter 4: Plasma Modelling Techniques. Chapter 5: The Study of Breakdown Caused by OFDM Signals analyses the effect of OFDM signals on electrical breakdown. Finally, the conclusions based on the main findings in this thesis will be presented in Chapter 6: Conclusion.

Chapter 2: Literature Review

2.1 Introduction

Electrical breakdown occurs when enough electron density is generated to form a conductive path between the electrodes. It is important to acquire required background knowledge of plasma physics. However, there is little work which is directly relevant to the topic of this thesis. The basic theory of gas breakdown was first developed by studying electrical breakdown in DC field for micro gaps where free electrons and positive ions move toward the anode and the cathode respectively. In this thesis, however, electrical breakdown is studied for relatively large gaps within radio frequency (RF) filters. DC discharge was the focus of early literature. In recent years, this focus has shifted to RF discharge. Most of the studies of RF discharge, however, are for specific low pressure gases or micro gaps or point-plane geometry [35-38]. While they provide some general understanding of electrical breakdown in gases, they are not directly relevant as the study in this thesis is for relatively large structures filled with air at atmospheric pressure.

The movement of electrons and ions is influenced by the frequency of the applied electric field. There is little research on the effect of signal frequency on breakdown behaviour. Semnani et al. [39] established that there are four distinct breakdown regions based on the signal frequency. However, the study in [39] is for micro/nanogap structures, so its results will not apply to our considered structure which has a relatively large gap between the electrodes. It will be shown in Chapter 5 that the carrier frequency of the signal has negligible effect on the breakdown behaviour.

In this chapter, previous relevant studies are reviewed. Section 2.2 presents the importance of plasma in gas discharge. The definition of plasma and its build-up are explained. Two main mechanisms which result in the generation and the loss of electrons are described. The initiation of electron avalanche within a parallel-plate structure is illustrated. Section 2.3 explains how CW and OFDM waveforms affect breakdown behaviour. This thesis focuses on the effect of OFDM signals on breakdown. This effect is compared to the effect caused by CW signals based on the PAPR of CW and OFDM signals. A previous study [30] of electrical breakdown caused by multicarrier signals is presented to show how the waveform affects the growth of free electrons. Section 2.4 analyses the Paschen curve which explains the relationship between breakdown threshold and gas pressure. A simulation result which shows the maximum energy

gained by electrons for a range of pressure is discussed. Section 2.5 discusses the effect of CW and OFDM signals on breakdown power of filters. The results in [15] are compared with the experimental data collected by an Australian manufacturer. To conduct the comparison, these results are plotted on the same graph. For the experimental data, the results of peak and average power of OFDM are plotted.

2.2 Plasma in Electrical Breakdown

Plasma is the aggregation of freely moving electrons and ions [40], as shown in Fig. 2.1. This collection of charged particles is, on average, electrically neutral. Electrical discharge is related to the build-up of plasma. This build-up is formed by collisions between electrons and gas molecules. There are two main types of collisions. The first type is elastic collision in which the impact results in little or no transfer of energy. The second type is inelastic collision which can emit a secondary electron.

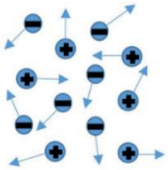

Fig. 2.1. Graphical depiction of plasma

At atmospheric pressure, the number of free electrons depends on two main mechanisms: ionization and attachment. Ionization is an inelastic collision when a high-energy electron collides with a molecule resulting in the release of an additional free electron from that molecule, as shown in Fig. 2.2(a). Attachment occurs when an electron attaches itself to a molecule to form an ion. Thus, a free electron is removed, as shown in Fig. 2.2(b). When the ionization rate exceeds the attachment rate, the electron gain is higher than the loss. As a result, breakdown will eventually take place if the electron density grows to a critical value.

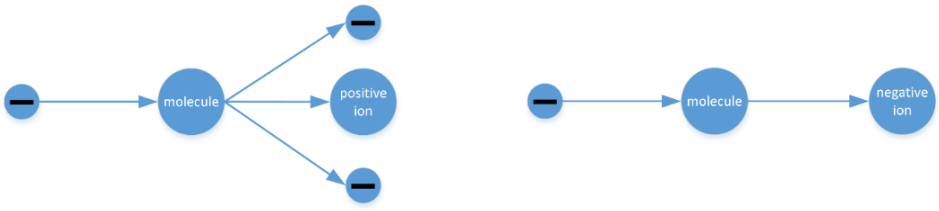

(a) (b)

Fig. 2.2. Main mechanisms causing changes in electron population: (a) ionization and (b) attachment

Fig. 2.3 shows the ionization process within a parallel-plate structure. It can be seen that the emitted electron resulted from one ionizing collision continues to collide with more gas molecules emitting more free electrons. This continuous build-up of electrons is called an electron avalanche. A continuous stream of avalanches is required to increase the electron density to a critical level. The critical electron density creates a conductive path between the electrodes for the current to flow through so that breakdown can occur.

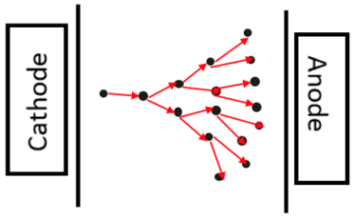

Fig. 2.3. A graphical depiction of electron avalanche in parallel plate structure

In this section, the definition of plasma, the two main mechanisms at atmospheric pressure, and the initiation of an electron avalanche, have been explained. This basic knowledge helps with the visualisation of the movement of particles during electrical breakdown.

2.3 Effect of Signal Waveform on Breakdown Behaviour

The rate of ionization and hence the electron population growth depends on the time-varying electric field resulting from the signal waveform. Free electrons accelerate in the direction of the field. When the signal is a sinusoidal waveform, these electrons move back and forth based on the temporal direction of the field caused by the signal. The electrons gain energy based on the instantaneous electric field strength. For RF signals, many collisions between free electrons and air molecules at atmospheric pressure take place in each half cycle of the signal frequency. These collisions result in losses in electron energy. Therefore, high electric field is required for electrons to gain sufficient energy to ionize. The nature of OFDM signals means that they have a higher PAPR than CW signals. This indicates that, given the same average power, the instantaneous electric field of OFDM signals can be much higher than that of CW signals. As a result, the ionization probability for OFDM signals is higher than that for CW signals. Thus, the waveform of OFDM signals is more likely to cause electrical breakdown. It will be shown in Chapter 5 that the probability of breakdown depends on the magnitude and the duration of a pulse in the signal envelope.

There is little research which considers electrical breakdown caused by a multicarrier signal. A multicarrier signal is formed by the summation of sinusoids of different frequencies [30]. For example, a two-carrier signal can be formed by summing two cosine waves. A general expression of a multicarrier signal $S(t)$ is given by [30]

$$S(t)=\sum_{n=1}^{N}\left(A_n\cos\left(2\pi f_n t+\varphi_n\right)\right),\quad n=1,2,...,N \tag{2.1}$$

where t is the time, n is the n^{th} carrier, A_n, f_n and φ represent the amplitude, carrier frequency and phase of n^{th} carrier respectively. Qian et al. [30] simulated a double-ridge waveguide breakdown using the spectral-element time-domain method. Fig. 2.4 shows the normalized electric field of a three-carrier signal as a function of time and the resulting electron density before and after gas breakdown, as found by Qian et al. [30]. During moments of high electric field strength, the number of ionizing collisions increases resulting in an increase in ionization rate. The electron density increases steeply as the generation rate of electrons is higher than the loss rate of electrons. During moments of low electric field strength, the electron density slowly declines as the loss rate of electron population is greater than the generation rate. Since the increase in electron density is greater than the decrease, the electron density steadily grows over time. This eventually results in a breakdown, as indicated by the attenuation of the electric field strength at 12 ns.

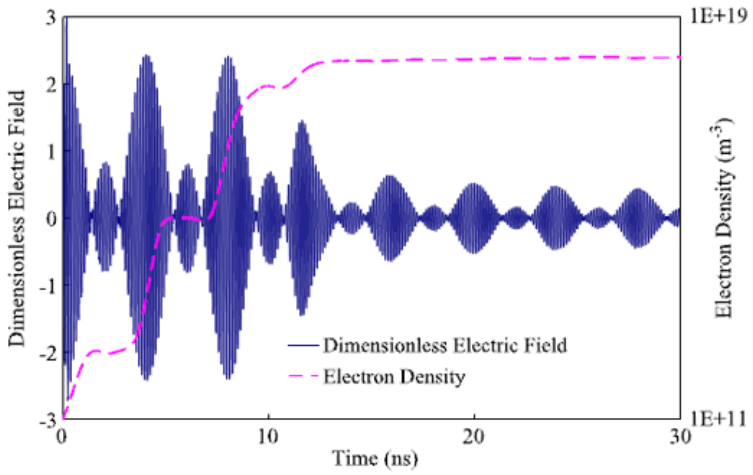

Fig. 2.4. Electron growth for a multicarrier waveform based on [30] (Copyright © 2016, IEEE), (DOI: 10.1109/LMWC.2016.2517156)

The effect of OFDM and CW signals on electrical breakdown has been briefly discussed. Compared to CW signals, the higher PAPR of OFDM can result in a higher probability of breakdown. Qian et al. [30] have shown that the growth of electron population depends on the

high and low amplitudes in a multicarrier waveform. This provides a basic idea of how OFDM waveform affects electrical breakdown.

2.4 The Paschen Curve

Breakdown behaviour depends on the gas pressure. There are two main types of breakdown: multipaction and ionization breakdown [41]. Multipaction breakdown is important in RF filters used for space applications as this mechanism takes place in vacuum. Ionization breakdown, which is the focus of this thesis, occurs at higher pressures than multipaction breakdown. The dependence of breakdown behaviour on pressure can be explained by using the Paschen curve. This curve [38, 42] shows the relationship between breakdown threshold and pressure of a gas. It is important to understand the Paschen curve because it helps explain how the movement of gas molecules affects the rate of ionization. The Paschen curve was first introduced in 1890s. An example of a Paschen curve is illustrated in Fig. 2.5 [38]. These results are based on the combination of both experimental and simulated data produced by Smith *et al.* [38]. The breakdown voltage is a strong function of the product of gas pressure p and the gap between two electrodes d. The breakdown voltage on the vertical axis is sometimes replaced with the electric field, while the pressure alone can be used on the horizontal axis when the gap length is fixed at a certain distance [43].

For a fixed distance between the electrodes, the Paschen curve can be described in terms of two different regions separated by the minimum of the curve. This can be explained in terms of the mean free path of the electrons. The mean free path of electrons is defined as the average distance between collisions of electrons and gas molecules at a given gas pressure. For the right-hand, high pressure region, there are more collisions between electrons and gas molecules. This results in significant energy losses in electrons, so the ionization probability decreases. Hence, a higher voltage is required to cause breakdown.

At low pressure, the electrons can move long distances before colliding with a gas molecule as the gas density is low. This results in a long mean free path. For the left-hand region of the Paschen curve, as the pressure decreases the mean free path of electrons becomes longer than the gap between the electrodes. In this case, there are fewer ionizing collisions between the electrodes. Therefore, a higher voltage is required to balance the energy losses and initiate breakdown.

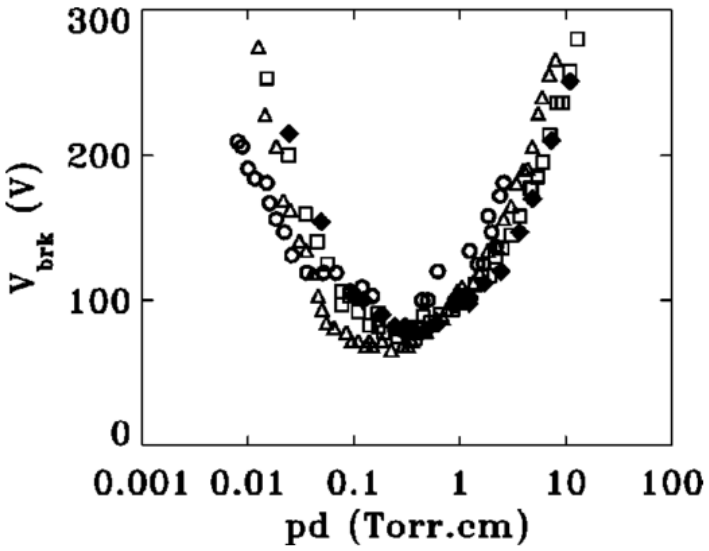

Fig. 2.5. Smith, H. B.'s Paschen curve (Reprinted from [38], with the permission of AIP Publishing.), (DOI: 10.1063/1.1531615)

The maximum energy gained by electrons in a gas depends on the mean free path. The gas pressure determines the mean free path, so it is important to understand how the pressure affects the maximum electron energy. Programs were written in MATLAB to calculate the maximum energy gained by electrons within the mean free path as the pressure varies. Fig. 2.6 shows the maximum electron energy as a function of gas pressure for a sinusoidal waveform. Let d_{max} be the maximum distance that electrons can travel due to the applied electric field. The electrons gain a constant maximum energy when the pressure is between 0 – 112 Torr. This is because, at these pressures, the mean free path is longer than d_{max}. As a result, the electrons gain maximum energy before collisions. The maximum energy falls when the pressure is greater than 112 Torr. At these pressures, the mean free path is shorter than d_{max}. As a result, the electrons gain less energy since collisions take place before the electrons reach d_{max}. When the pressure increases further, the maximum energy falls as the mean free path decreases. Since the electrons gain lower energy at higher pressures, the rate of ionization decreases. Therefore, higher voltages are required to cause breakdown, as shown in Fig. 2.5.

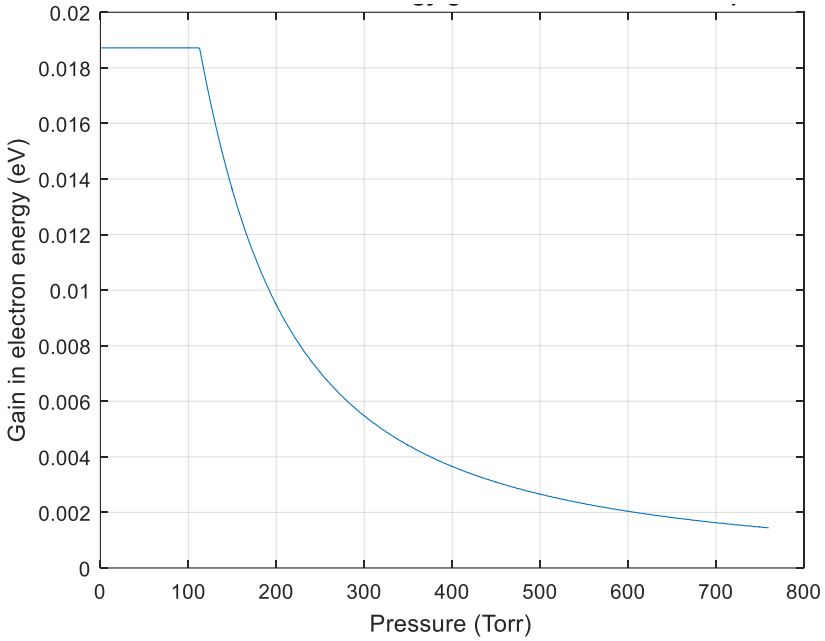

Fig. 2.6. Maximum pressure-dependant energy of an electron before collisions

The Paschen curve describes the relationship between breakdown threshold and gas pressure. Electrons gain less energy at high pressures due to high number of collisions, so high breakdown threshold is resulted. This section has described how breakdown behaviour depends on the gas pressure.

Radio Frequency Systems (RFS) is a worldwide leading provider of innovative wireless and broadcast infrastructure products and solutions. This manufacturer provides a range of products including antennas and filters. RFS conducted experiments to measure the breakdown power of filters as the air pressure varies. The measurements were done based on [15, 33]. In their research laboratory, they found that the results of breakdown power as a function of air pressure for OFDM signals were not as expected and not well understood. These results will be shown in the following section.

2.5 The Effect of CW and OFDM Signals on Breakdown Power

RFS use the fact that at lower air pressures breakdown occurs at lower voltages to test their high power filters. This allows them to test the overload performance of very high power filters using their lower powered DVB transmitter. A DVB signal of known average power is input to the filter and the air pressure gradually lowered until breakdown occurs. In the experiment, the setting for signal generation was as follows: 2K FFT mode, 64-QAM constellation, guard

interval of 1/8, and bandwidth of 8 MHz. For single carrier systems it has been found that the variation of breakdown power with pressure is accurately predicted by the Paschen curve.

RFS conducted an experiment to investigate the effect of OFDM signals on breakdown power of the filter. The experimental results were compared with the results of breakdown power caused by a CW signal. The results for a CW signal was plotted by RFS based on [15]. Fig. 2.7 shows the results of breakdown power caused by a CW signal as a function of pressure.

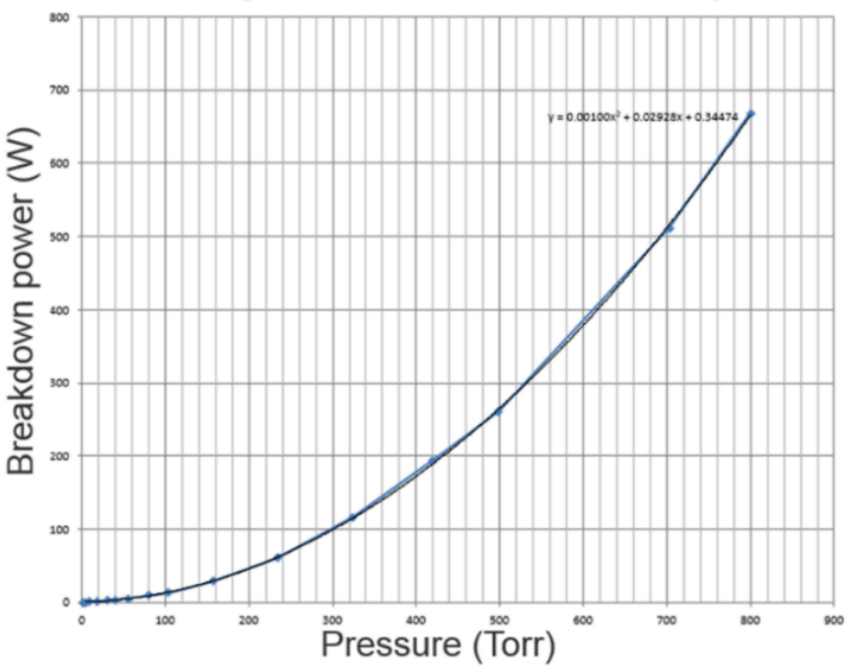

Fig. 2.7. A Paschen curve for a CW signal based on [15] (Copyright © 1999, IEEE), (DOI: 10.1109/22.809005)

Fig. 2.8(a) and (b) show the experimental results collected by RFS for the peak power and average power at breakdown, respectively, for an OFDM signal. In the experiment, a power meter was used to measure the peak and average powers. Fig. 2.8(a) and (b) also show the results in Fig. 2.7 for comparison. The peak power and average power of the OFDM signal at the lowest pressure are used as reference points for the comparison. The values of breakdown power for the CW signal are scaled by factors of 2500 and 90 respectively so that the reference points are on the Paschen curve. In Fig. 2.8(a), from 200 Torr, the peak power of the OFDM signal starts to level off and deviate from the Paschen curve. Whilst in Fig. 2.8(b), when the pressure increases, it can be seen that the average power of the applied OFDM signal also increases. The relationship appears to be similar to that for a CW signal. This was a surprising result as it was assumed that breakdown would depend on the peaks of the OFDM signal rather than its average power.

Fig. 2.9 shows the resulting PAPR of the OFDM signal as a function of average input power, based on the experimental data. This shows that as the average power of the signal increases the PAPR decreases. This is probably because the transmitter is reaching its maximum power output and is distorting the peaks of the signal. It will be shown later that this distortion may explain the experimental results.

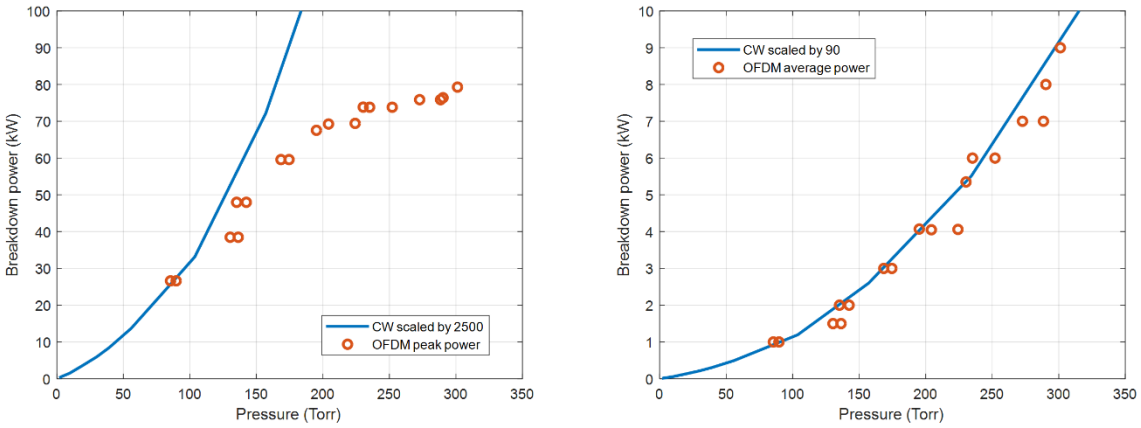

(a) (b)

Fig. 2.8. Comparison of a Paschen curve for a CW signal and OFDM (a) peak power and (b) average power (based on experimental data by RFS)

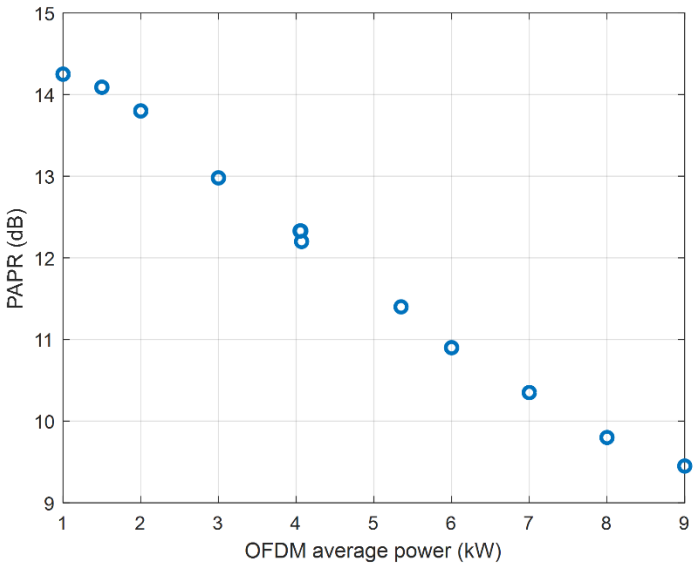

Fig. 2.9. The change in the PAPR of OFDM as a function of average power (based on experimental data by RFS)

In this section, the effect of an OFDM signal on breakdown threshold has been compared to the effect of a CW signal. The Paschen curve describes the breakdown behaviour for a CW and the relationship between breakdown power and pressure. Whilst the RFS data based on the

average power follows a similar trend, that of the peak power deviates strongly at high pressure values. RFS also showed that the relationship of PAPR is pressure dependant. This starts to give a mechanism to understand the deviation from the Paschen curve seen in the peak power data, however it does not give a full explanation. The following chapters will examine theoretically the relationship between OFDM signal and the likelihood of breakdown, focusing on the role played by peaks in the signal (Chapter 5), and through this approach provide some understanding of this effect.

2.6 Conclusions

In this chapter, relevant studies have been reviewed. The basic knowledge of plasma physics and previous theoretical and simulation results have been analysed in relation to the problem of electrical breakdown. Plasma is the aggregation of electrons and ions. At atmospheric pressure, two main mechanisms in air are ionization and attachment. The ionization causes the electron avalanche in gas. The breakdown behaviour of OFDM signals is different from that of CW signals because OFDM has a higher PAPR. It has been shown that for a multicarrier waveform, the electron density increases during moments of high electric field strength and falls when the electric field is low. In addition, the importance of the Paschen curve has been described. An experimental investigation conducted by RFS has been described. The RFS data of the peak power deviates from the Paschen curve. An explanation of this effect will be provided in the following chapters.

Chapter 3: OFDM Theory

3.1 Introduction

To generate OFDM signals, it is essential to first understand the modulation process of OFDM so that the simulations can produce the correct waveform. In this chapter, the basic theory of OFDM is presented. The modulation process of OFDM for signal transmission will be described.

3.2 Description of OFDM Theory

OFDM theory is studied to broadly understand the signal characteristic and how the signal is generated in a transmission system. Fig. 3.1 shows the process of generating each OFDM symbol in the transmitter. The use of cyclic prefix has been ignored in the OFDM simulation as it has little effect on the outcome of electrical breakdown. A more extensive description of OFDM theory can be found in [2, 44].

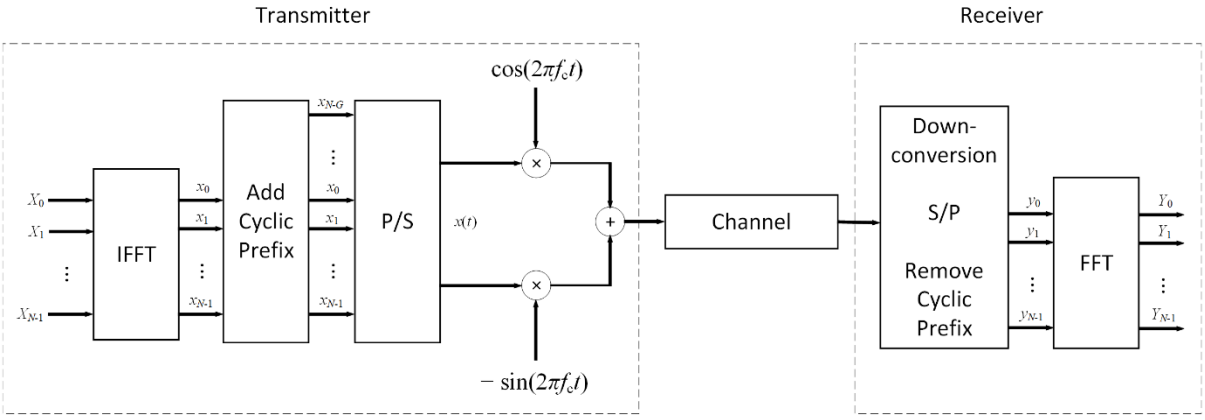

Fig. 3.1. Block diagram of OFDM communication system based on [2] (Copyright © 2009, IEEE), (DOI: 10.1109/JLT.2008.2010061)

3.2.1 IFFT

The inverse fast Fourier transform (IFFT) transforms an array of frequency-domain data into a vector of time-domain data by using the definition of the inverse discrete Fourier transform:

$$x_m = \frac{1}{\sqrt{N}} \sum_{k=0}^{N-1} X_k e^{\frac{j2\pi km}{N}}, \quad \text{for } 0 \le m \le N-1 \tag{3.1}$$

The input array to the IFFT is the complex vector $\boldsymbol{X} = [X_0\ X_1\ X_2\ \ldots\ X_{N-1}]^T$ and has length N where N is the number of subcarriers in each OFDM symbol. Each of the elements of $\boldsymbol{X}$ is represented by X_k (the data to be carried on the k^{th} subcarrier). The output of the IFFT is a time-domain vector $\boldsymbol{x} = [x_0\ x_1\ x_2\ \ldots\ x_{N-1}]^T$ where x_m is m^{th} sample. The frequency domain and time domain data samples are illustrated in Fig. 3.2. The time intervals between transmission of the elements of the time domain vector $\boldsymbol{x}$ depend on aspects of the transmitter design including the bandwidth of the signal and the length of the cyclic prefix. Following the terminology in the DVB standard [1] we refer to this at the 'elementary period', T_E. For DVB, T_E is 109 ns, 125 ns, 146 ns, and 175 ns for 8 MHz, 7 MHz, 6 MHz and 5 MHz channels respectively [1].

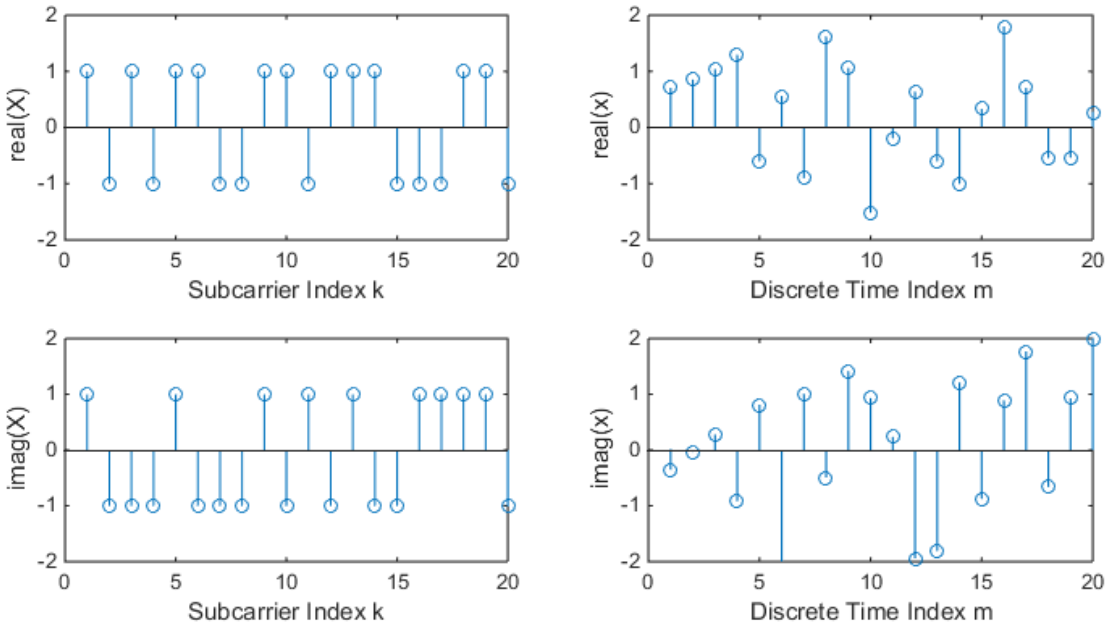

Fig. 3.2. Frequency domain data (left column) and time domain samples (right column)

3.2.1.1 Mapping

To obtain $\boldsymbol{X}$, data symbols are randomly generated in parallel and then mapped using M complex quadrature amplitude modulation (QAM). Gray mapping is used in the constellations. For the following simulations in this chapter, 16-QAM is considered. For 16-QAM, the values of symbols vary from 0 to 15 (0 to $M - 1$). Each of the elements after mapping becomes a complex number which represents a QAM constellation point, as shown in Fig. 3.3.

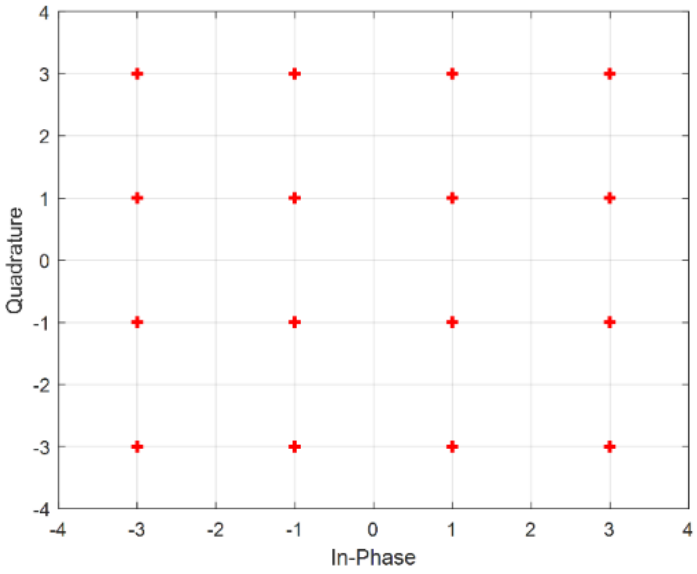

Fig. 3.3. Constellation points for data symbol vector ***X*** after mapping

3.2.1.2 Normalization

Before going through the IFFT, ***X*** is normalized to have a unity average power by the following process. Let a data symbol vector α be [0 1 2 3] where each symbol is mapped to constellation points represented by β (mapped symbols). The power for transmitting corresponding data symbol is $|\beta|^2$. If the sum of all these powers, represented by γ, is multiplied by a normalization coefficient c, the total power will have a value of 4, which means the average power is 1. To achieve a unity average power, ***X*** must be multiplied by square root of the normalization coefficient.

3.2.1.3 Oversampling

The next technique applied to the inputs of IFFT is interpolation by oversampling. Two inputs of IFFT, 0 and $N/2$, are nulled as the interpolation technique does not work for these values. If an oversampling factor is I, the input to IFFT is extended by adding $N(I-1)$ zeroes in the middle of the vector. This is called zero padding. $I \geq 4$ is typically used to accurately interpolate the time-domain OFDM signal.

There are three factors that need to be multiplied to the output of IFFT in order to maintain the unity power of the signal. The first factor is $N^{1/2}$ since MATLAB defines IFFT as

$$x_m = \frac{1}{N}\sum_{k=0}^{N-1} X_k e^{\frac{j2\pi km}{N}}, \quad \text{for } 0 \le m \le N-1 \tag{3.2}$$

in which it is different by a factor of $1/N^{1/2}$ from (3.1). The second factor is $I^{1/2}$ which compensates for the power reduction caused by the zero padding. Finally, the output of IFFT is multiplied by a factor of $[N/(N-2)]^{1/2}$ to compensate for the power reduction caused by nulling the two elements of the input of the IFFT as mentioned above. The effect of oversampling is shown in Fig. 3.4 where $I = 4$. Let $\boldsymbol{x} = [x_0\ x_1\ x_2\ \ldots\ x_{N-1}]^T$ be the vector of samples without oversampling and $\boldsymbol{x}^{\boldsymbol{I}}_{\mathbf{over}} = [\,X^I_{\text{over},0}\ X^I_{\text{over},1}\ X^I_{\text{over},2}\ \ldots\ X^I_{\text{over},NI-1}\,]^T$ be the vector of samples when oversampling is applied where I is the degree of oversampling. In Fig. 3.4, the blue points represent $\boldsymbol{x}$ whereas the circles show $\boldsymbol{x}^{\boldsymbol{I}}_{\mathbf{over}}$.

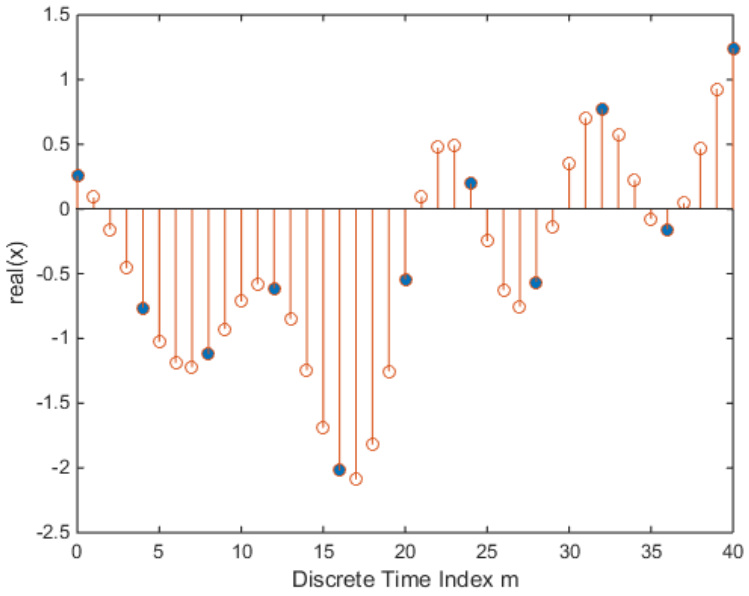

Fig. 3.4. Samples with (circles) and without (blue points) oversampling

3.2.1.4 Statistics of OFDM Signals

The distribution of pulse height in the OFDM waveform determines the probability of electrical breakdown, which will be discussed in Chapter 5. The signal samples represented by x_m at the output of the IFFT have a similar distribution to Gaussian distribution because the operation of IFFT results in adding up many independently modulated subcarriers to which the central limit theorem applies. A Gaussian signal is used to represent the real and imaginary components of an OFDM signal and the power is calculated. The power is the sum of squares of two Gaussian signals. As a result, the distribution of the power is chi-squared distribution [45]. Fig. 3.5 shows

complementary cumulative distribution function (CCDF) of power of the OFDM signal. Large power peaks occur relatively rarely. For example, only one in a thousand values is approximately more than 8 dB above the mean power of the signal.

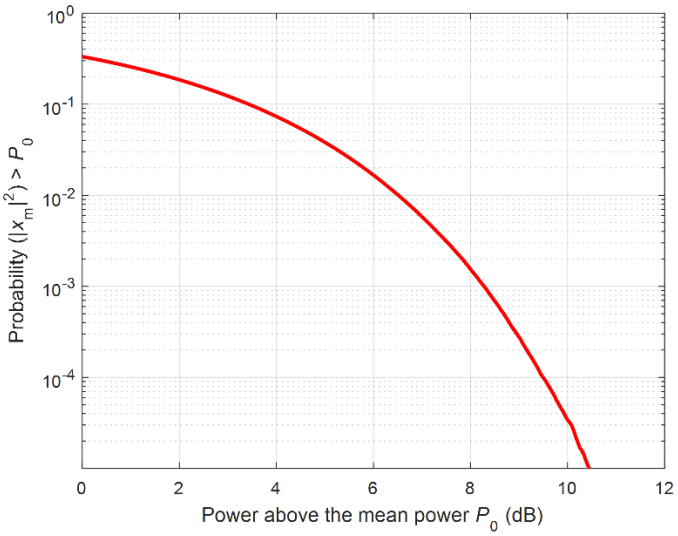

Fig. 3.5. Complementary cumulative distribution function of power of OFDM signal

3.2.2 Up-Conversion

Each OFDM symbol needs to be up-converted before transmitting through an RF channel. The output of the IFFT is parallel-to-series (P/S) converted, followed by an up-conversion process. The transmitted signal is given by

$$\begin{aligned} s(t) &= \mathrm{Re}\{x(t)\}\cos(2\pi f_c t) - \mathrm{Im}\{x(t)\}\sin(2\pi f_c t) \\ &= \mathrm{Re}\{x(t)e^{2\pi f_c t}\} \end{aligned} \tag{3.3}$$

where $x(t)$ is a complex baseband signal, and f_c is the carrier frequency of the transmitted signal. Fig. 3.6 shows the OFDM signal spectrum after up-conversion where f_c = 666 MHz. Fig. 3.7 shows the power of an up-converted OFDM signal within one symbol period where the average power is 1 W. It can be seen that the peak power of this signal is much greater than the mean power. In this case, the peak power is more than 10 dB above the mean. Fig. 3.8(a) and (b) respectively show the baseband oversampled signal and its equivalent RF signal within the first 1 μs of the waveform in Fig. 3.7. The peaks in Fig. 3.8(a) correspond to the peaks in Fig. 3.8(b). Fig. 3.9(a) and (b) show the first 0.1 μs of the waveform in Fig. 3.8(a) and (b) respectively. When the baseband oversampled signal is up-converted, the envelope of its equivalent RF signal contains many cycles of the carrier frequency of the signal.

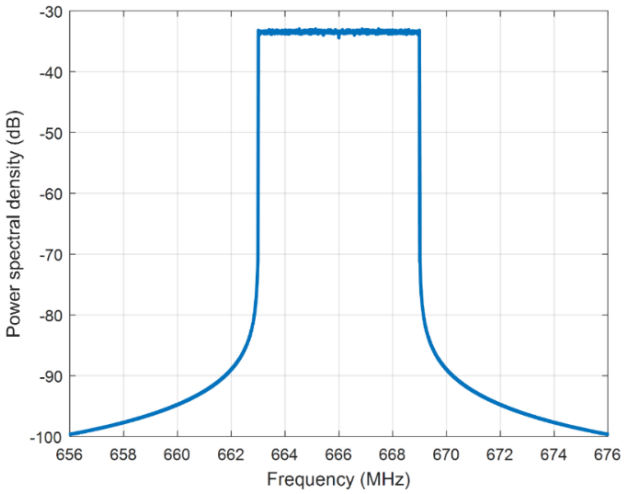

Fig. 3.6. Power spectral density plot of an up-converted OFDM signal with f_c = 666 MHz

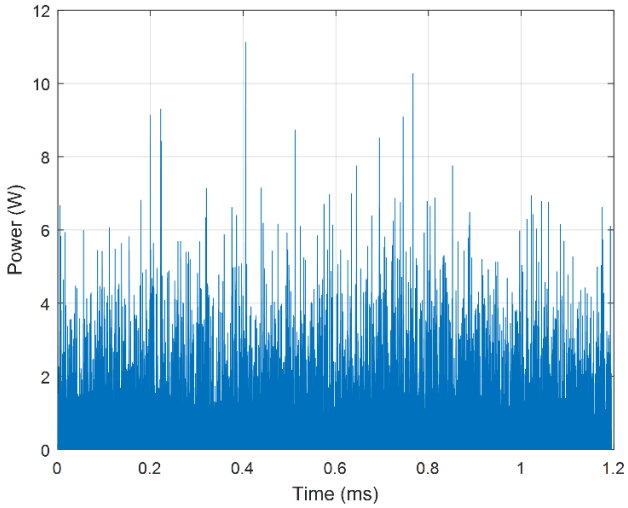

Fig. 3.7. An RF OFDM signal within one symbol period

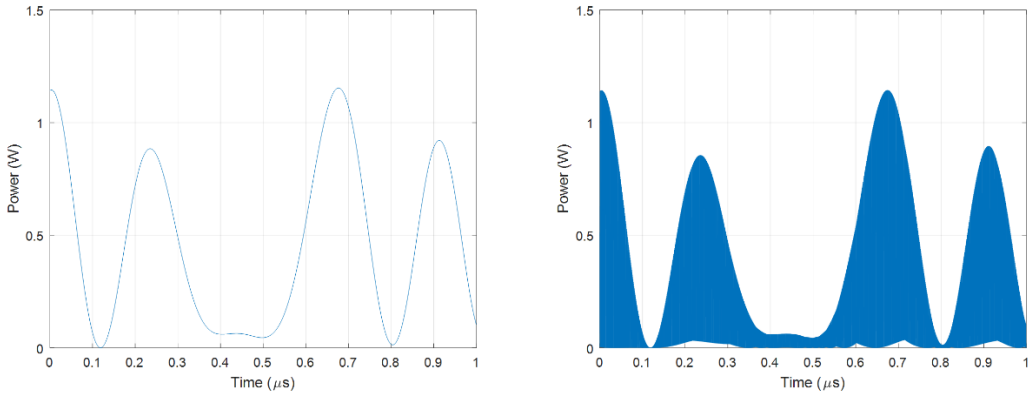

(a) (b)

Fig. 3.8. (a) The baseband oversampled signal and (b) the equivalent RF signal within the first 1 μs of the waveform in Fig. 3.7

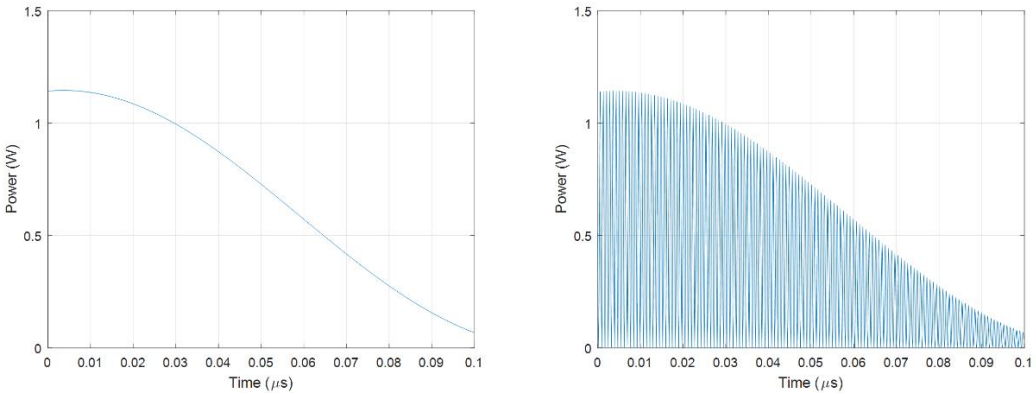

(a) (b)

Fig. 3.9. (a) The baseband oversampled signal and (b) the equivalent RF signal within the first 0.1 μs of the waveform in Fig. 3.8

3.3 Summary of Different Concepts of OFDM Signal

In this section, the different concepts of an OFDM signal, which will be referred to in the later chapters, have been described. Without oversampling, the output of the IFFT is a vector of baseband, $\boldsymbol{x}$. When oversampling is applied, the output of the IFFT is $\boldsymbol{x}^{I}_{\mathbf{over}}$. Fig. 3.10(a) shows the samples of $\boldsymbol{x}$ (red circles) and the resulting continuous baseband signal (blue). It can be seen that a large sample in $\boldsymbol{x}$ results in a large peak in the continuous signal. The continuous signal is up-converted to form an equivalent RF signal known as a passband signal. Fig. 3.10(b) shows the equivalent passband signal of the continuous baseband signal in Fig. 3.10(a).

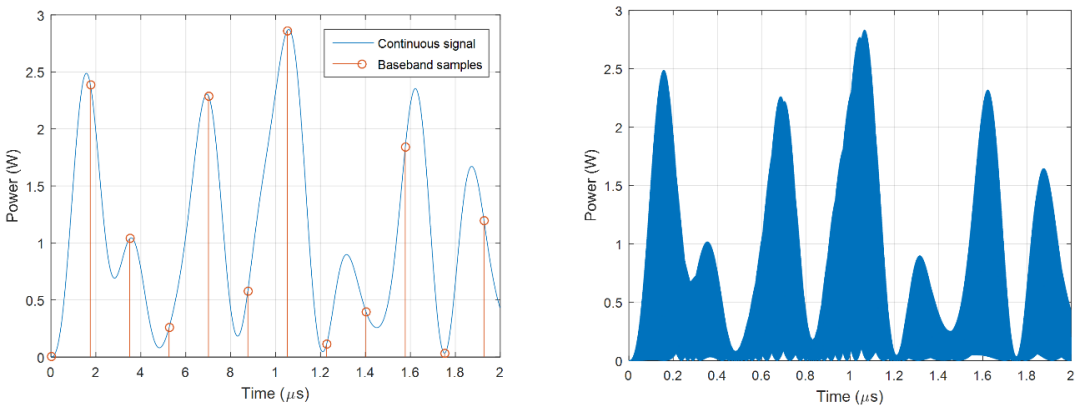

(a) (b)

Fig. 3.10. (a) The baseband samples before oversampling (red circles) and the resulting continuous baseband signal (blue), and (b) the equivalent passband signal

3.4 Conclusions

In this chapter, the basic theory of OFDM has been presented. The modulation process of OFDM for signal transmission has been described with corresponding simulation results. The baseband oversampled signal and its equivalent RF signal which contains many cycles of the carrier frequency of the up-converted signal have been shown. The different concepts of OFDM signal have been summarised.

Chapter 4: Plasma Modelling Techniques

4.1 Introduction

The RFS experiments (Fig. 2.8) show that the values of peak power of OFDM deviate from the Paschen curve as the air pressure increases. This thesis seeks to explain this deviation. To achieve this, a plasma modelling technique is required, which is capable of studying the breakdown behaviour caused by OFDM signals. Breakdown occurs when the electron density grows high enough to form a conductive path for the current to flow through. As such, the growth of electron density when the time-varying electric field is caused by an OFDM signal needs to be calculated. At atmospheric pressure, the electron density in air is caused by ionization and attachment processes which can be modelled in several ways including Monte Carlo simulation [46-54] and the use of ionization kinetics equations [55].

Monte Carlo simulation captures the physics of particles under an applied field based on the collisions between electrons and gas molecules. As a result, it gives a better understanding of the problem. The simulation was focused in the early stage of this research. There are two versions of Monte Carlo simulation: the basic Monte Carlo simulation and the more sophisticated Monte Carlo simulation. The simulation method of each version will be discussed. The comparison between our simulation results and the results from previous studies is conducted to validate the functionality of the simulation. In addition, the effect of various signals on breakdown behaviour is studied. The reasons why Monte Carlo simulation is not suitable to use for the study in this thesis will be explained.

An alternative approach which overcomes the limitations of Monte Carlo techniques is the use of the ionization kinetics equations. A limitation of these equations is that they assume that fields and particle densities are uniform throughout the volume considered so cannot take into account the geometry of particular devices. The use of these equations is very computational efficient, so they are suitable for use with OFDM signals.

Section 4.2 describes the basic version of Monte Carlo simulation that was developed during this project and our study of how CW signals affect the electron mean energy. Section 4.3 explains the more sophisticated version of Monte Carlo simulation that has been developed in previous studies [46-48, 56-60] and why it is not suitable to use for the study in this thesis. Section 4.4 shows the derivation of ionization kinetics equations.

4.2 Monte Carlo Simulation

In the early stage of this research, MATLAB was used to develop a Monte Carlo simulation based on previous studies [36, 37, 49, 61] to model the interactions between electrons and gas particles within a parallel-plate structure. In this section, a method overview of this simulation is described, followed by our MATLAB simulation results which are in a good agreement with those presented in the reviewed literature.

4.2.1 Method Overview

This section describes how the Monte Carlo simulation is structured. All calculations for the simulation are carried out at each time step Δt. First, the position and speed of each electron is calculated. Various effects of collisions are determined by finding a collision probability P_c given by

$$P_c\left(t_k\right) = 1 - e^{-\nu_T\left[\upsilon\left(t_k\right)\right]\Delta t} \tag{4.1}$$

where t_k is the time of k^{th} time step, ν_T is the total collision frequency of the collisions between electrons and neutral gas molecules, and $\upsilon(t_k)$ is the velocity of electron. If a collision takes place, the type of the collision such as elastic, exciting and ionizing collisions is then determined based on the probabilities given in Fig. 4.1. The electron energy is either unchanged or lost based on this collision type. When an electron loses its energy due to collisions, its speed decreases. In the simulation the direction of electron movement after any collision is randomly generated. For an ionizing collision, a secondary electron is released from the molecule it collided with. The secondary electron obtains half of the original energy of the colliding electron. The ionizing collisions also release positive ions. A cloud of these ions forms a space charge which can distort the applied electric field. The calculations of electric field are carried out at the end of each Δt taking in account the effects of both the applied electric field and the space charge. In the simulation, it was found that the effect of the space charge was negligible. All calculations in the current Δt are used to determine the electron movement for the next Δt i.e. the position $x(t_{k+1})$

$$x\left(t_{k+1}\right) = x\left(t_k\right) + \upsilon\left(t_k\right)\Delta t + 0.5\left(e/m\right)E\left(\Delta t\right)^2 \tag{4.2}$$

and speed $\upsilon(t_{k+1})$

$$\upsilon(t_{k+1}) = \upsilon(t_k) + (e/m)E\Delta t \tag{4.3}$$

where e is the electron charge, and m is the electron mass.

Fig. 4.1(a) shows the collision frequency as a function of electron energy for different types of collision. This data is used to calculate the collision probability. The sum of elastic, ionizing and exciting collision frequencies results in the total collision frequency. It can be seen that the elastic collision frequency is higher than the ionizing and exciting collision frequencies when the electron energy is low. When the electron energy is high, the ionizing and exciting collision frequencies are higher than the elastic collision frequency.

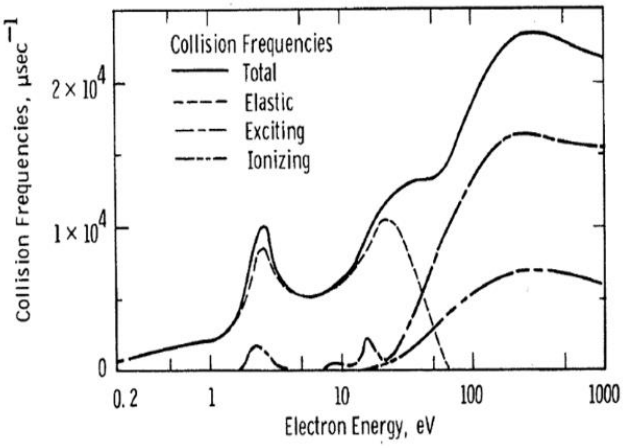

Fig. 4.1. Collision frequencies for nitrogen at 1 Torr based on [49] (Reprinted figure with permission from [49] ©1972 American Physical Society.), (DOI: https://doi-org.ezproxy.lib.monash.edu.au/10.1103/PhysRevA.5.794)

4.2.2 Simulation Results

To validate the method of Monte Carlo simulation, MATLAB was used to duplicate the results of mean electron energy and first ionization coefficient α_i from [49] for a DC signal with the applied electric field of 150 V/cm. The first ionization coefficient is given by [49]

$$\alpha_i = \frac{\log\left[N_e(t)/N_e(t_0)\right]}{\left[x_{\text{avg}}(t) - x_{\text{avg}}(t_0)\right]} \tag{4.4}$$

where N_e is the number of electrons, x_{avg} is the average electron position, and t_0 is the time for the electron avalanche to reach a steady state. The electron mean energy is the sum of energy gained by electrons divided by the total number of electrons. The results of mean electron energy and first ionization coefficient are for a parallel-plate structure filled with nitrogen at

0.5 Torr. The collision frequencies at 0.5 Torr are given by the product of the collision frequency at 1 Torr and a factor of 0.5. The simulation starts with 50 electrons.

Fig. 4.2(a) and (b) show the mean electron energy and the first ionization coefficient, respectively, as a function of time. Fig. 4.3 shows the results from [49] for comparison where the left vertical axis shows the first ionization coefficient and the right vertical axis shows the electron mean energy. In Fig. 4.2(a), the mean electron energy approaches 12.5 eV which is similar to that in Fig. 4.3. In Fig. 4.2(b), the first ionization coefficient reaches a constant value of 1.75 cm^{-1}. This value is in a good agreement with the result in Fig. 4.3.

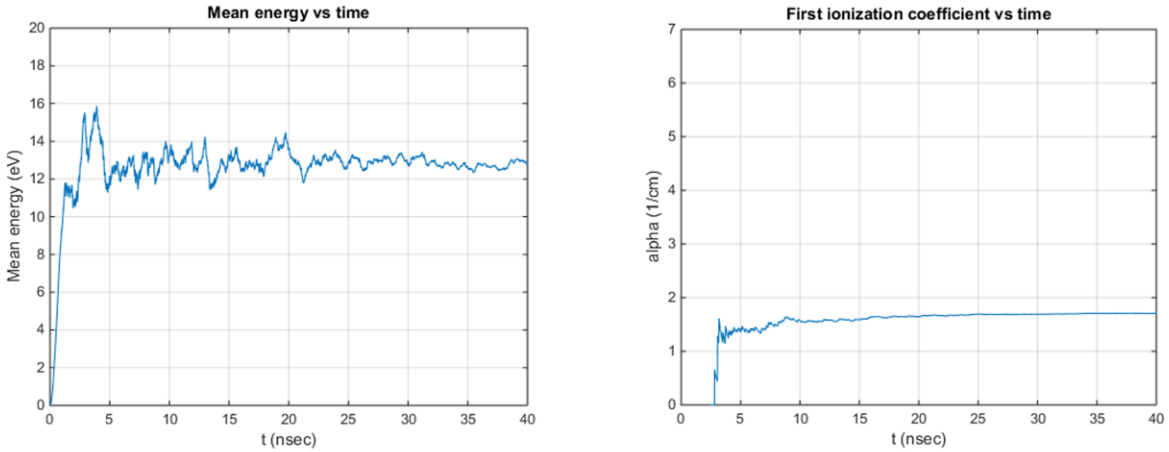

(a) (b)

Fig. 4.2. (a) Mean energy and (b) first ionization coefficient calculated using MATLAB

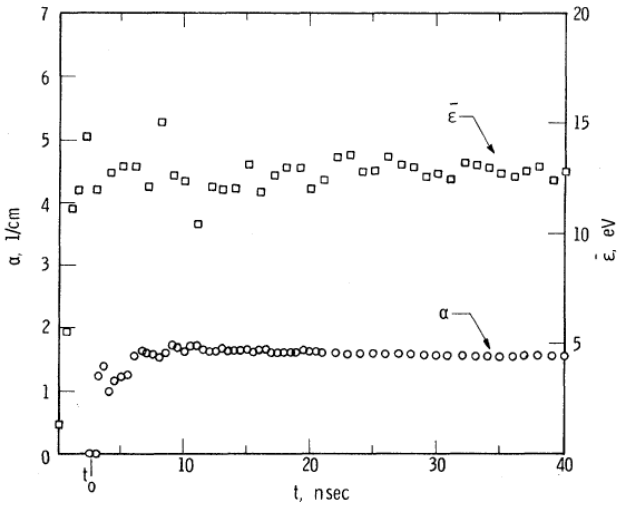

Fig. 4.3. Mean energy and first ionization coefficient from [49] (Reprinted figure with permission from [49] ©1972 American Physical Society.), (DOI: https://doi-org.ezproxy.lib.monash.edu.au/10.1103/PhysRevA.5.794)

In addition, our simulation results for drift velocity υ_d are compared to the results from [49]. The drift velocity is given by [49]

$$\upsilon_d = \frac{\left[x_{\text{avg}}(t) - x_{\text{avg}}(t_0)\right]}{(t - t_0)} \tag{4.5}$$

Fig. 4.4 shows the drift velocity as a function of the ratio of electric field to pressure, E/p, where the blue dots represent our MATLAB simulation results. In the figure, the circles and the solid lines indicate the simulation results and the experimental results, respectively, from [49]. The drift velocity is calculated for six values of E/p where the pressures are 0.2 Torr for E/p = 1000 and 600, 0.5 Torr for E/p = 300, and 1 Torr for E/p = 150, 100 and 70. The collision frequencies at 0.2 Torr are given by the product of the collision frequency at 1 Torr and a factor of 0.2. In Fig. 4.4, it can be seen that our results are in a good agreement with the benchmark results as our calculated drift velocities (blue dots) are approximately equal to those from [49] (circles).

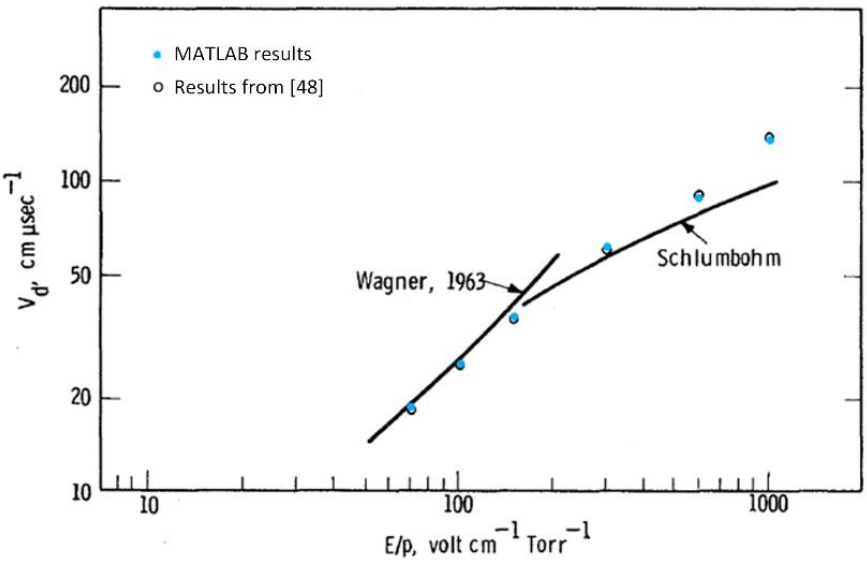

Fig. 4.4. Calculated and experimental values of drift velocity υ_d as a function of E/p (Reprinted figure with permission from [49] ©1972 American Physical Society.), (DOI: https://doi-org.ezproxy.lib.monash.edu.au/10.1103/PhysRevA.5.794)

4.2.3 The Effect of CW Signals on Electron Mean Energy

Monte Carlo simulation was next used to investigate the effect of a CW signal on the mean energy of electrons. The mean energy of electrons was calculated for a sinusoidal signal with

the signal frequency of 25 MHz. Fig. 4.5 and Fig. 4.6 respectively show the amplitude of the signal waveform and the mean electron energy as a function of time. Fig. 4.5(a) and Fig. 4.6(a) show the results within the first 40 ns of the simulation while Fig. 4.5(b) and Fig. 4.6(b) show the results within the first 180 ns of the simulation. It can be seen that the mean energy varies at twice the signal frequency. In the first 40 ns of the simulation, the electron population is low. In Fig. 4.6(a), the change in the mean energy is not stable as the calculations are based on a low number of free electrons. After the simulation runs for 180 ns, more electrons are created by the ionizing collisions. In Fig. 4.6(b), the mean electron energy becomes more stable as the calculations are based on a large electron population.

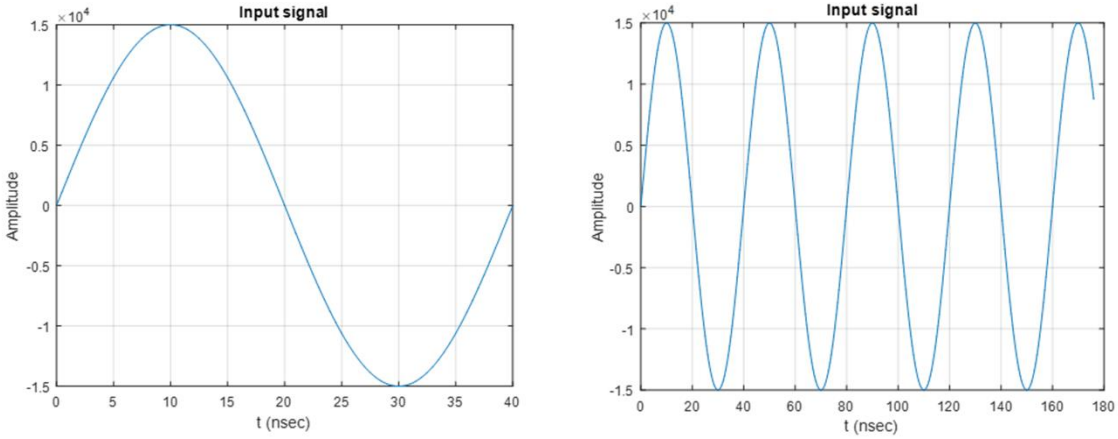

(a) (b)

Fig. 4.5. The applied voltage waveform within the first (a) 40 ns and (b) 180 ns of the simulation

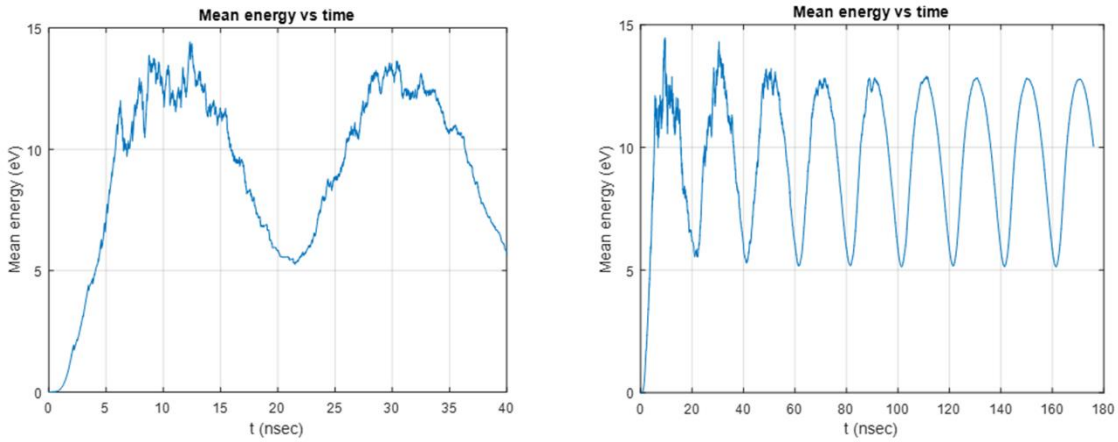

(a) (b)

Fig. 4.6. The mean energy of electrons within the first (a) 40 ns and (b) 180 ns of the simulation

Next, the effect of the signal frequency on the mean electron energy was studied. Monte Carlo simulation is used to calculate the mean electron energy caused by a sinusoidal signal with different signal frequencies. Fig. 4.7(a) and (b) show the mean electron energy as a function of time at 666 MHz and 13.56 MHz respectively. At 666 MHz, the electrons travel shorter distances than compared to those at 13.56 MHz due to the shorter cycle period at the higher frequency. This results in a lower maximum energy gained by the electrons. As a result, the mean energy in Fig. 4.7(a) is lower than that in Fig. 4.7(b).

In Fig. 4.7(a), it takes approximately 200 ns for the mean energy to reach a steady state while it is 100 ns in Fig. 4.7(b). This is because the rate of ionization is lower at the higher frequency, so the generation rate of free electrons is lower. As a result, it takes longer for the electron population to reach a high enough level for a steady state.

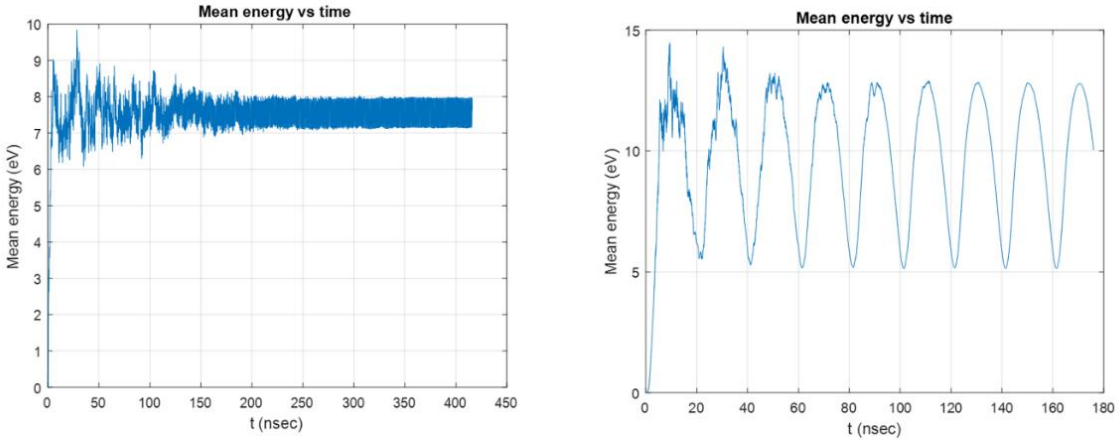

(a) (b)

Fig. 4.7. The mean electron energy when the signal frequency is (a) 666 MHz and (b) 13.56 MHz

This version of Monte Carlo simulation provided a good understanding of the interactions between particles in gases as it captures the behaviour of the plasma under an applied electric field. Although the simulation was capable of generating reasonable results, it was only computationally feasible for an extremely low pressure. A much more efficient simulation was required for modelling the electron avalanche at atmospheric pressure. This brings us to the second version of Monte Carlo simulation which will be described in the next section.

4.3 More Sophisticated Monte Carlo Simulation

4.3.1 Method Overview

A more computationally efficient form of Monte Carlo simulation known as particle-in-cell/Monte Carlo collisions (PIC/MCC) has been developed in previous studies described in the literature [46-48, 56-60] for a number of applications. In an early stage, Birdsall [46] and his team developed a PIC/MCC code for low-pressure, low-density plasmas. This code was then improved by Kawamura *et al.* [58] to run faster for low-pressure RF discharges so that it can be beneficial to plasma processing machine designers and experimentalists. For this research, the more recent version of this code was used to simulate electrical breakdown caused by OFDM signals. PIC/MCC simulation provides high computational efficiency and full detail of gas discharge phenomena. This is a significant improvement over the simple Monte Carlo simulation described in Section 4.2.

In the PIC scheme, the particles are overlayed using a mathematical grid for which charge density is computed, as shown in Fig. 4.8 [46]. Fig. 4.9 [46] illustrates the computing sequence for PIC/MCC simulation. At the start of the simulation, the velocity and the position of a particle are known and used to produce the charge density ρ at the grid points. This charge density is then used to obtain the electric field E on the grid by solving field equations. Once the field is calculated, the electric field strength is used to advance the velocity and the position of the particle by applying the equations of motion. The particle is either absorbed, reflected or absorbed emitting another particle based on imposed boundary conditions. The MCC scheme is applied to model elastic and inelastic collisions. The new values of velocity and position of the particle are then used to repeat the computing sequence of PIC/MCC simulation for the next time step.

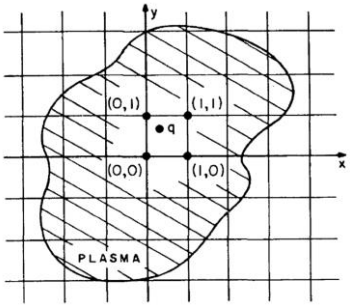

Fig. 4.8. A mathematical grid set into the plasma region for measuring charge density based on [46] (Copyright © 1991, IEEE), (DOI: 10.1109/27.106800)

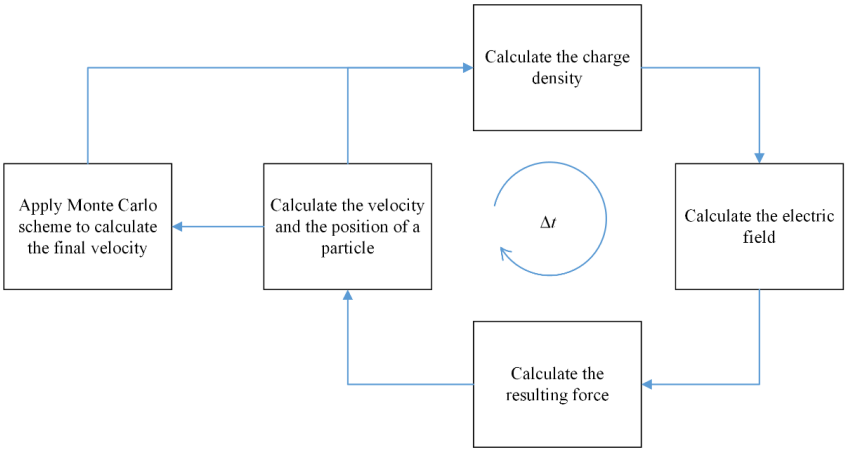

Fig. 4.9. The flow chart for an explicit PIC/MCC scheme based on [46] (Copyright © 1991, IEEE), (DOI: 10.1109/27.106800)

The object-oriented plasma device one (OOPD1) code developed by the Plasma Theory and Simulation Group (PTSG) at university of California, Berkeley [62] is accessible for simulating plasma using the method of PIC/MCC. One advantage of this code is that it allows users to simulate a multicarrier input signal, which is important for this research.

4.3.2 Simulation Results

At the early stage of this research, OOPD1 code was used to duplicate various results from [63]. The simulations were to produce results which were in a good agreement with the benchmark results so that the use of OOPD1 code for this thesis could be verified. The simulation was for a parallel-plate structure filled with oxygen gas at 50 mTorr. The gap between the electrodes was 4.5 cm. The input signal was a sinusoidal waveform with an amplitude of 222 V at 13.56 MHz of signal frequency. In the simulation, our results using OOPD1 code were collected at an earlier simulation time than in [63], so the results are slightly different. The simulations only aimed to confirm the general trend of the results which should be in a good agreement with the benchmark results. The simulations were based on case 5 (using a full reaction set for oxygen) in [63]. In Fig. 4.10 - Fig. 4.14, the lefthand figures show the results in [63] whereas the righthand figures show our results using OOPD1 code.

Fig. 4.10 shows the potential ϕ profile across the gap between the electrodes, x. In Fig. 4.10(a), the maximum potential reaches 102.55 V while it is 105 V in Fig. 4.10(b). Fig. 4.11 shows the electron temperature T_e profile across x. It can be seen that T_e = 3.5 V at x = 0 cm in Fig. 4.11(a). Fig. 4.11(b) shows that T_e = 4.4 V at x = 0 cm. Fig. 4.12 shows the electron energy probability function (EEPF) as a function of electron energy at the center of x. The shapes of

EEPF profiles are similar in both figures. In Fig. 4.12(a), the peak value of EEPF is 1×10^{13} $eV^{-3/2}m^{-3}$ while it is 1×10^{12} $eV^{-3/2}m^{-3}$ in Fig. 4.12(b). Fig. 4.13 demonstrates the electron heating rate *J.E* profile across *x*. The electron heating rates in both figures are approximately equal at the center of the gap. Fig. 4.13(b) shows lower values at $x = 1.5$ cm and at $x = -1.5$ cm compared to those in Fig. 4.13(a). Lastly, the particle density *n* profiles across *x* for electron and three oxygen ions (O^-, O^+ and O_2^+) are compared. In Fig. 4.14(b), the curves representing the densities of electron (blue), O^- (white), O^+ (green) and O_2^+ (yellow) have different colours compared to those in Fig. 4.14(a). The overall results of the density profiles in both figures are similar. To sum up, our simulation results generated by OOPD1 code are in a good agreement with the results in [63].

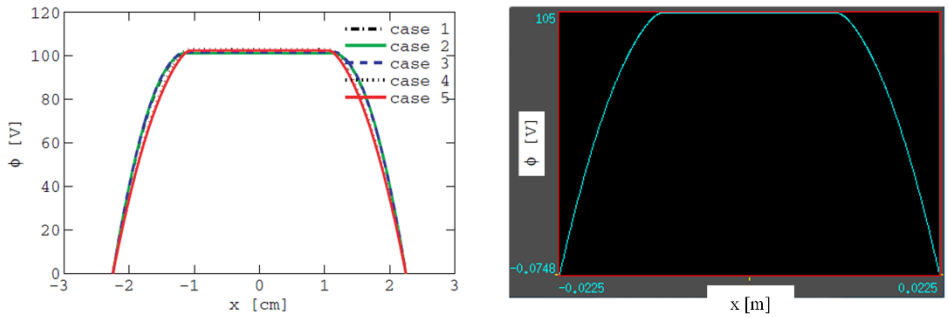

(a) (b)

Fig. 4.10. Potential profile within the gap, based on (a) the results from [63] and (b) our simulation results using OOPD1 code (© IOP Publishing. Reproduced with permission. All rights reserved), (DOI: 10.1088/0963-0252/22/3/035011)

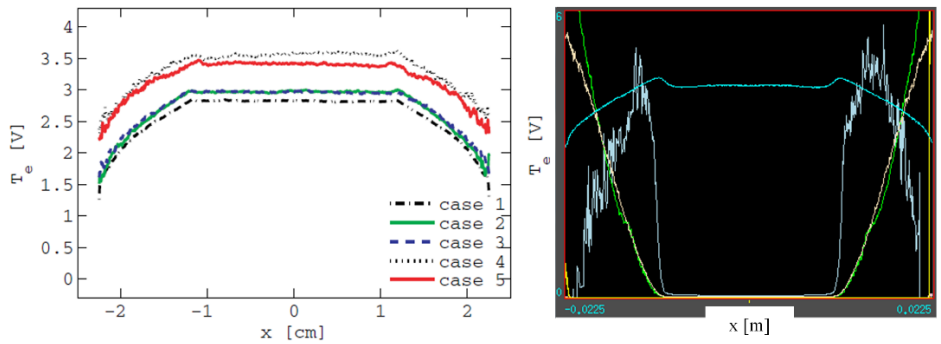

(a) (b)

Fig. 4.11. Electron temperature profile based on (a) the results from [63] and (b) our simulation results using OOPD1 code (© IOP Publishing. Reproduced with permission. All rights reserved), (DOI: 10.1088/0963-0252/22/3/035011)

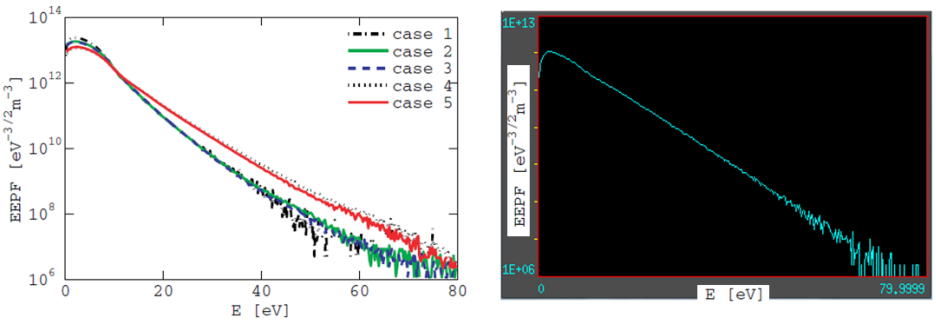

(a) (b)

Fig. 4.12. Electron energy probability function based on (a) the results from [63] and (b) our simulation results using OOPD1 code (© IOP Publishing. Reproduced with permission. All rights reserved), (DOI: 10.1088/0963-0252/22/3/035011)

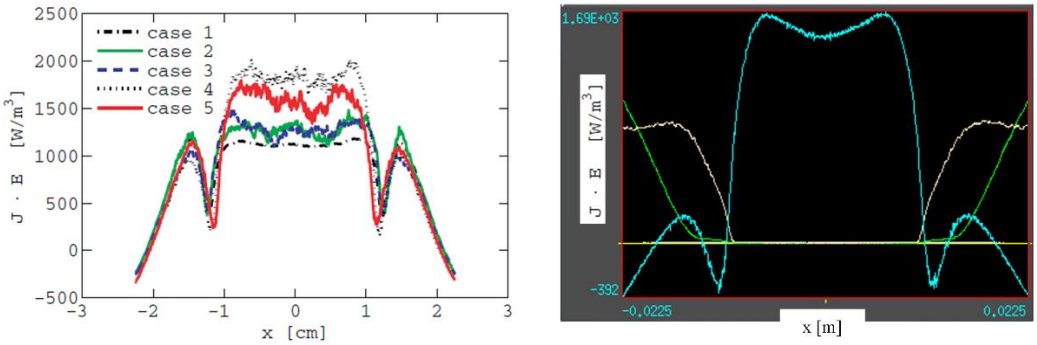

(a) (b)

Fig. 4.13. Electron heating rate based on (a) the results from [63] and (b) our simulation results using OOPD1 code (© IOP Publishing. Reproduced with permission. All rights reserved), (DOI: 10.1088/0963-0252/22/3/035011)

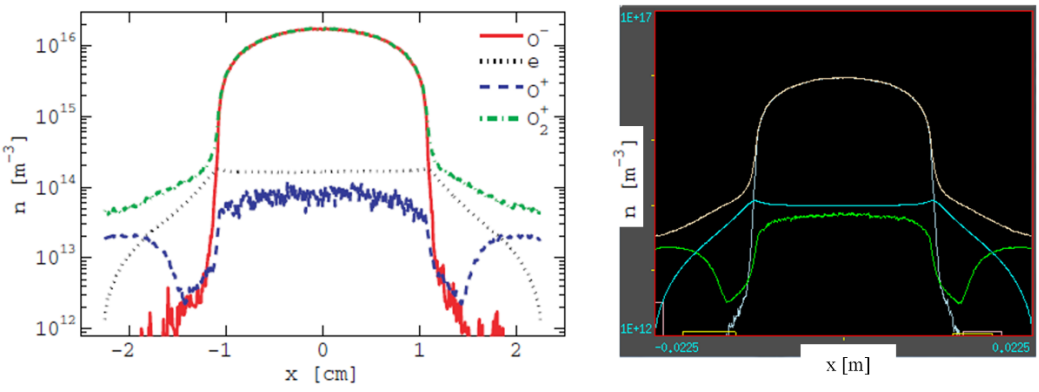

(a) (b)

Fig. 4.14. Density profiles of particles based on (a) the results from [63] and (b) our simulation results using OOPD1 code (© IOP Publishing. Reproduced with permission. All rights reserved), (DOI: 10.1088/0963-0252/22/3/035011)

OOPD1 code was also used to simulate the effect of multicarrier waveforms on the growth of electron population to compare with the benchmark results in [30]. Fig. 4.15 - Fig. 4.17 respectively show CW, 2-carrier and 3-carrier signals as a function of time and the resulting electron population. Fig. 4.15(a), Fig. 4.16(a) and Fig. 4.17(a) show the input voltage and the number of free electrons generated using OOPD1 code. Fig. 4.15(b), Fig. 4.16(b) and Fig. 4.17(b) [30] show the dimensionless electric field (scale on left) and the electron density (scale on right). Note that the electron population and density are plotted using a logarithmic scale. The simulations were to simply show the general trend of electron population growth based on the number of carriers in the signal as the structure geometries used in the two simulations were different. In Fig. 4.15(a) and (b), the voltage is set above the breakdown level. As a result, the electron population increases as its growth rate is higher than its loss rate. In Fig. 4.16(a) and (b), the electron population increases during moments of high voltage and falls during moments of low voltage. Similar behaviour can be observed in Fig. 4.17(a) and (b). To sum up, the electron population simulated by OOPD1 code follows the general growth trend of the results in [30].

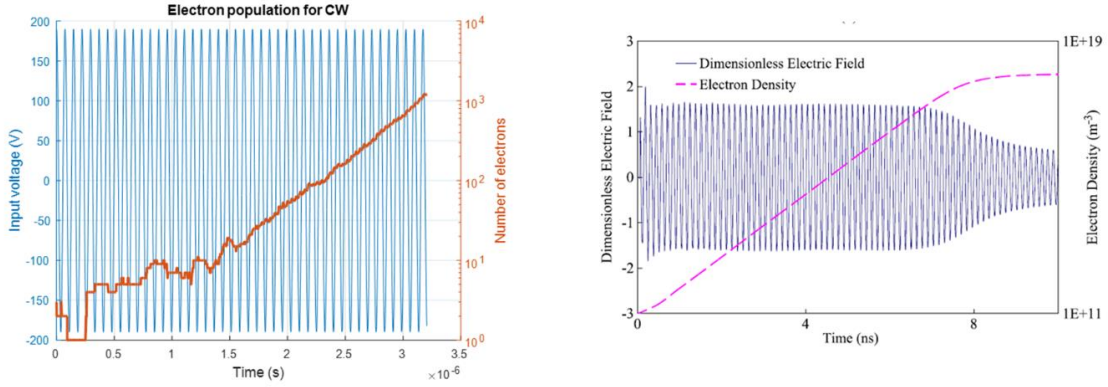

(a) (b)

Fig. 4.15. A CW signal and the resulting electron population: (a) our results using OOPD1 code and (b) the results from [30] (Copyright © 2016, IEEE), (DOI: 10.1109/LMWC.2016.2517156)

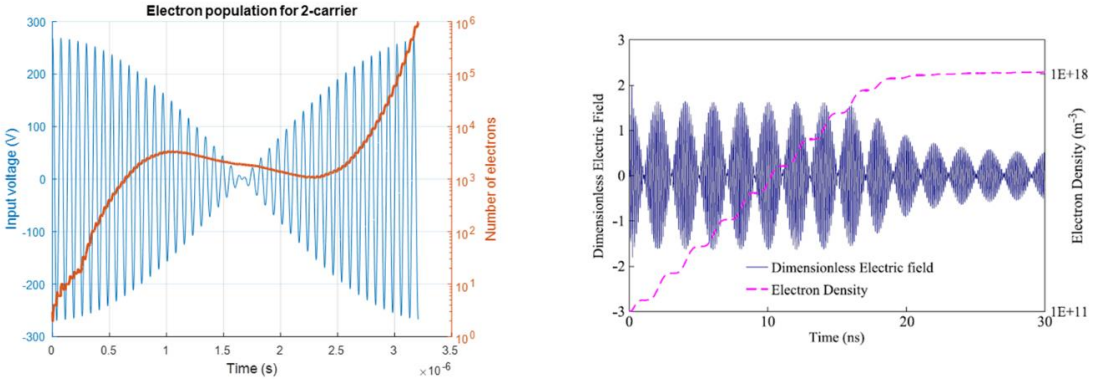

(a) (b)

Fig. 4.16. A 2-carrier signal and the resulting electron population: (a) our results using OOPD1 code and (b) the results from [30] (Copyright © 2016, IEEE), (DOI: 10.1109/LMWC.2016.2517156)

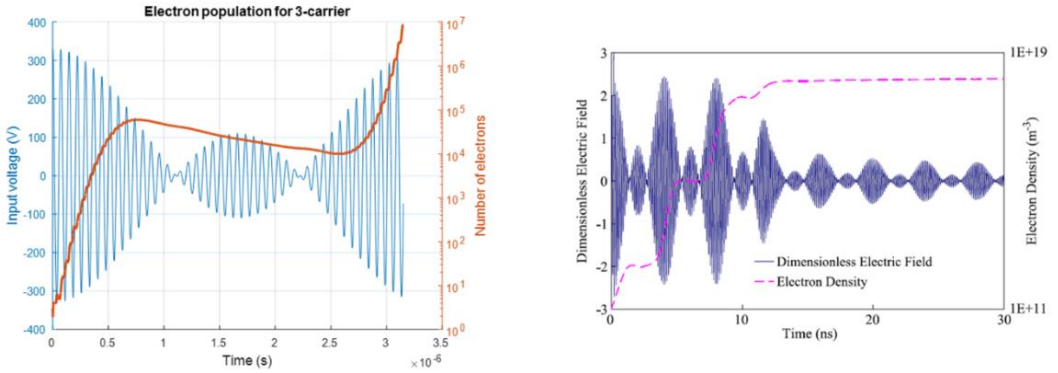

(a) (b)

Fig. 4.17. A 3-carrier signal and the resulting electron population: (a) our results using OOPD1 code and (b) the results from [30] (Copyright © 2016, IEEE), (DOI: 10.1109/LMWC.2016.2517156)

4.3.3 Encountered Problems of OOPD1 Code

The OOPD1 code had a number of issues which were not well understood. Fig. 4.18 shows the voltage of the input sinusoidal signal as a function of time (seconds), generated by OOPD1 code. In the figure, it can be seen that the waveform begins to behave like a DC signal at around t = 0.7 ms. The cause of this behaviour is unknown. In addition, the simulation automatically stopped at approximately t = 0.97 ms. The same simulation was run several times and the

results showed that the simulation stopped after t = 0.97 ms for each run. This might be due to the memory limitation of the computer used to run the simulation.

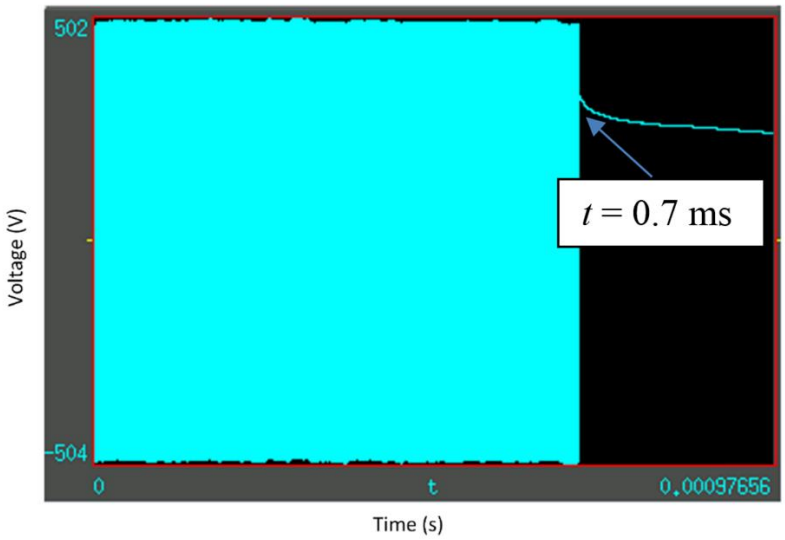

Fig. 4.18. OOPD1 applied voltage waveform showing an unknown behaviour

Although PIC/MCC simulation is much more efficient than the initial form of Monte Carlo simulation, it is still computationally intensive as many calculations are required at each time step. In our simulations using OOPD1 code, the gas pressure was restricted to an extremely low value so that a reasonably fast simulation was possible as the lower pressure reduced the number of calculations at each time step. However, when the pressure was increased to atmospheric pressure (760 Torr), the simulation became prohibitively slow. This is because more collisions between the electrons and gas molecules take place at the higher pressure, which results in more calculations. For the case of OFDM signals, the probability of large power peak which causes breakdown is extremely low, so long OFDM waveforms must be simulated. As a result, PIC/MCC simulation is not feasible for this study.

The OOPD1 code was written by other people, so it is difficult for us to find the source of the issues in the code. The simulation consists of many files for compilation and the code is written in C language. Many files were checked to find the cause of the issues that were encountered. Moreover, this code has been written for limited uses. This might explain why the simulation runs well for an extremely low pressure but not for atmospheric pressure. In addition, the code has not been written to take full advantage of supercomputers to run faster. As a result, the issue of slow simulation speed cannot be resolved.

In conclusion, a much simpler approach is needed to model the growth of electron population in air when the applied electric field is the result of an OFDM signal. This simpler

approach is the use of ionization kinetics equations which will be explained in the following section.

4.4 Ionization Kinetics Equations

4.4.1 Derivation of Ionization Kinetics Equations

The ionization kinetics equation as shown in (4.6) was used in [31] to calculate breakdown due to a multicarrier signal, but no clear derivation or source of the equation was given. An extensive search of the literature also revealed no clear derivation. In the following we show how the equation can be derived based on [64-66].

The ionization kinetics equation calculates the instantaneous density of free electrons in a fixed volume filled with air at atmospheric pressure. The simulations of electron density are based on the equation [31]

$$v = \left(6.4\times10^{4}\, p\right)\left\{\left[\frac{P(t)}{P_{\mathrm{b}}^{\mathrm{CW}}}\right]^{8/3} - 1\right\} \tag{4.6}$$

where v is the net rate of generation of free electrons, p is the pressure measured in Torr, P is the instantaneous power, t is the time, and $P_{\mathrm{b}}^{\mathrm{CW}}$ is the CW breakdown threshold which can be determined either theoretically or experimentally based on the geometry of the device. At atmospheric pressure, the value of p is 760 Torr. When $P \ll P_{\mathrm{b}}^{\mathrm{CW}}$, $v \approx -100p^2$. Equation (4.6) is derived in [64] using the effective electric field E_e. The expression for E_e is derived from the product of the instantaneous electric field $E(t)$ and the drift velocity $\upsilon_d(t)$. $E(t)$ is expressed by [65]

$$E(t) = E_0 \sin(\omega t) \tag{4.7}$$

where E_0 is the amplitude of electric field, and ω is the angular frequency. $\upsilon_d(t)$ is obtained by solving the differential equation for the net average velocity of electrons

$$\frac{\mathrm{d}\upsilon_d(t)}{\mathrm{d}t} = \left(\frac{e}{m}\right)E_0 \sin(\omega t) - \nu_c \upsilon_d(t) \tag{4.8}$$

where e is the electron charge, m is the electron mass, and ν_c is the average collision frequency and is assumed to be independent of the electron energy. The solution to (4.8) is given by [65]

$$\upsilon_d(t) = \frac{(e/m)E_0\left[\nu_c \sin(\omega t) - \omega\cos(\omega t)\right]}{\left(\nu_c^2 + \omega^2\right)} \tag{4.9}$$

The product of $E(t)$ and $\upsilon_d(t)$ is then written and simplified as

$$\upsilon_d(t).E(t) = 2\mu E_e^{\,2}\left[\sin^2(\omega t) - \frac{\omega}{2\nu_c}\sin(2\omega t)\right] \tag{4.10}$$

where $\mu = e/(m\nu_c)$, and $E_e = E_0/\{2[1+(\omega/\nu_c)^2]\}^{1/2}$. The expression for E_e was used by Bisbing *et al.* [66] to derive an empirical function for ν using the method of curve fitting to experimental data. This empirical function is approximated as [64]

$$\frac{\nu}{p} = 4\times10^7\left[\frac{(E_e/p)}{10^2}\right]^{5.33} - 6.4\times10^4 \tag{4.11}$$

Equation (4.6) is derived by rewriting (4.11) to obtain the ratio of two effective electric fields E_{e1} and E_{e2} with corresponding ν_1 and ν_2 respectively. This ratio is simplified as

$$\left(\frac{E_{e1}}{E_{e2}}\right)^{5.33} - 1 = \frac{(\nu_1 - \nu_2)}{\left(\nu_2 + 6.4\times10^4\, p\right)} \tag{4.12}$$

If E_{e2} is the CW breakdown field, then $\nu_2 \approx 0$. Then (4.12) becomes

$$\nu = \left(6.4\times10^4\, p\right)\left[\left(\frac{E_e}{E_b^{\,CW}}\right)^{5.33} - 1\right] \tag{4.13}$$

Equation (4.13) was then used by Jordan *et al.* [31] to derive the expression for P_b^{CW} by replacing E_e/E_b^{CW} with $(P/P_b^{CW})^{0.5}$, as shown in (4.6). The rate of change in electron density is given by

$$\frac{dn}{dt} = \nu_i(t)\,n - \nu_a(t)\,n + J \tag{4.14}$$

where n is the electron density, ν_i is the ionization frequency, ν_a is the attachment frequency, and J represents a source of free electrons from cosmic rays. In (4.14), the difference between the ionization frequency and the attachment frequency is the net rate of generation of free electrons, so $\nu = (\nu_i - \nu_a)$. Equation (4.6) is used to calculate ν which is then used to compute the instantaneous change in electron density based on (4.14).

4.4.2 Effect of Carrier Frequency on P_b^{CW}

Depending on the country, DVB-T signals are typically transmitted on either the very-high frequency (VHF) band or the ultra-high frequency (UHF) band. The carrier frequencies for these television (TV) frequency bands are between 54 MHz and 806 MHz, so it is important to know whether P_b^{CW} varies within this frequency range. P_b^{CW} is proportional to the squared breakdown electric field, E_{rms}^2, where E_{rms} (V/cm) can be approximated by [67]

$$E_{rms} \approx 32\left(p^2 + 2f_c^2\right)^{1/2} \tag{4.15}$$

In (4.15), f_c is measured in GHz, and p = 760 Torr at atmospheric pressure. Using (4.15), it can be shown that from 54 MHz to 806 MHz, there is an increase of only 1.1×10^{-4} % in E_{rms}. Thus, P_b^{CW} is approximately constant over the TV frequency bands.

4.4.3 Electron Density Growth Rate

The growth rate of electron density depends on the factor $(P/P_b^{CW})^{8/3}$ in (4.6). Fig. 4.19 shows $(P/P_b^{CW})^{8/3}$ as a function of P. In the simulation, P_b^{CW} was set to 1 W. In Fig. 4.19, it can be seen that when P above P_b^{CW} increases, the factor $(P/P_b^{CW})^{8/3}$ increases significantly indicating that the electron density can rise significantly when $P/P_b^{CW} \geq 1$. This effect plays a significant role in causing electrical breakdown when large peaks in an OFDM signal occur.

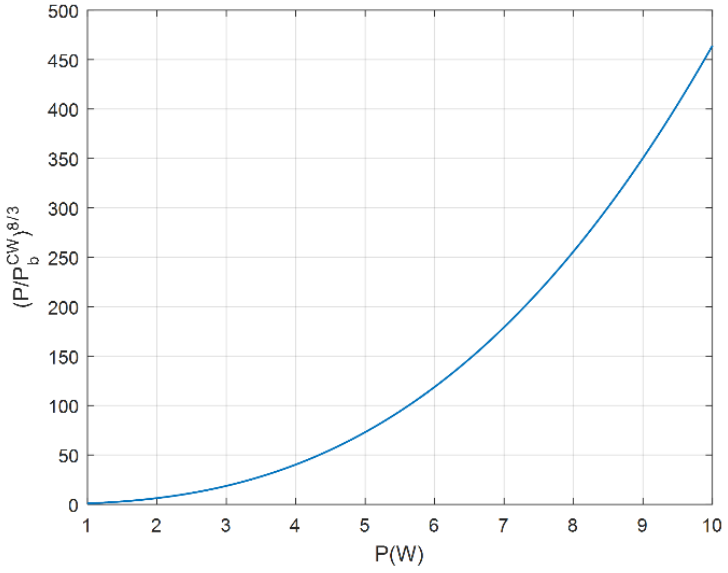

Fig. 4.19. $(P/P_b^{CW})^{8/3}$ of the ionization kinetics equation

4.5 Conclusions

In this chapter, two ways of modelling the statistics of ionization and attachment have been presented. One way is the use of Monte Carlo simulation. The basic and improved versions of Monte Carlo simulation have been described along with various simulation results to compare with benchmark results. A number of studies on the effect of various signals on breakdown behavior have been conducted. Another way to model the ionization and attachment is the use of ionization kinetics equations which have been derived from the fundamental equations. The use of these equations for this research study has been validated. In addition, the simulation results show that the electron density can rise significantly when $P/P_b^{CW} \geq 1$.

Monte Carlo simulation provides high accuracy in modelling the physics of electrons in gases. It iteratively calculates the velocity and the position of electrons for each relatively small time step. Moreover, it can capture some features of device geometry for higher accuracy. However, Monte Carlo simulation is extremely intensive in computation terms as many processes take place at each time step. This becomes less feasible when dealing with OFDM waveforms as the probability of peaks which result in electrical breakdown is extremely low, so long waveforms must be simulated. The use of ionization kinetics equations is a lot less computationally intensive as it is based on a relatively simple formula. In addition, these equations can be used with an OFDM signal. Therefore, the ionization kinetics equations are suitable for studying electrical breakdown caused by OFDM signals.

Chapter 5: The Study of Breakdown Caused by OFDM Signals

5.1 Introduction

The signal waveform plays an important role in the growth of electron density. In an OFDM system, a continuous baseband signal is up-converted to form a passband signal where the envelope of the passband signal contains many cycles of the carrier frequency of the signal, as described in Chapter 3. In this chapter, the ionization kinetics equations are used to calculate the growth of electron density when the electric field is due to a single burst of sinusoidal signal. The length of burst of a given amplitude required to cause breakdown is calculated. It is shown that high power bursts of length of the order of the elementary period of a DVB-T signal can cause breakdown. Next, simulations are performed to determine the probability of the width and height of peaks in a typical sample function of a European standard DVB-T signal. It is shown that high peaks also have lengths of the order of the elementary period of a DVB-T signal. A combination of these two findings are then used to explain results of the RFS experiments.

Because breakdown depends on the very short term statistics of the waveform, breakdown is likely to occur only when there are two consecutive high amplitude baseband samples. It is shown that the amplitude of a peak caused by two of these samples also depends on the phase difference between the samples and suggested that new digital signal processing algorithms for reducing the probability of breakdown may be possible.

The carrier frequency of a DVB-T signal varies based on the channel requirement. The effect of the frequency within the TV frequency bands on electrical breakdown is studied. The resulting electron density is investigated when the carrier frequency of the signal is 473 MHz and 803 MHz respectively.

Section 5.2 presents the effect of a burst of sinusoidal signal on electrical breakdown. Section 5.3 discusses the properties of peaks in DVB-T signals. Section 5.4 demonstrates the effect of the carrier frequency of the signal on electrical breakdown.

5.2 The Effect of a Burst of Sinusoidal Signal

Electron density strongly depends on the form of the signal waveform, so it is important to understand how the electron population varies based on the magnitude and the duration of

peaks in the OFDM signal. Equations (4.6) and (4.14) from Section 4.4 were used to calculate the electron density. Equation (4.6) shows that the change in electron density depends on P/P_b^{CW}. When $P/P_b^{CW} > 1$, ν is a positive value indicating that the ionization rate is higher than the attachment rate. The electron density will increase at a rate ν. When $P/P_b^{CW} < 1$, ν becomes negative. In this case, the attachment rate is greater than the ionization rate. As a result, the electron density will fall. In this section, we analyse the growth in electron density resulting from a burst of sinusoidal signal of constant amplitude.

Firstly, the effect of peak power of the burst, P_p, on the growth of electron population is analysed. The ionization kinetics equations are used to calculate the instantaneous density of free electrons for the signal with a carrier frequency of 666 MHz (UHF). Each cycle of the carrier frequency of a passband signal has a period T. P/P_b^{CW} varies sinusoidally at twice the carrier frequency, so there are two cycles of P/P_b^{CW} per T. The magnitudes of electron density depend quite strongly on the external source of free electrons, J. (See equation (4.14) for definition of J.) In the simulation, when $P/P_b^{CW} < 1$ for a long period of time relative to the attachment time, the electron density fell to a base level determined by J. The value of J was selected so that the base level was around 1 cm^{-3}. The following results were generated using MATLAB. Fig. 5.1(a) and (b) show the normalized instantaneous power P/P_b^{CW} (blue) as a function of time and the resulting electron density (dark orange) within two cycles of the carrier frequency of the signal. The electron density increases and decreases in each cycle of P/P_b^{CW}. In Fig. 5.1(a), the peak power is high enough for the average ionization rate to exceed the average attachment rate. As a result, the electron density steadily grows. In Fig. 5.1(b), the peak power is lower than that in Fig. 5.1(a). The ionization gains are less than the attachment losses, resulting in a steady decrease in electron density. Since the peak power of the burst affects the growth of electron density, electrical breakdown depends on the magnitude of a pulse.

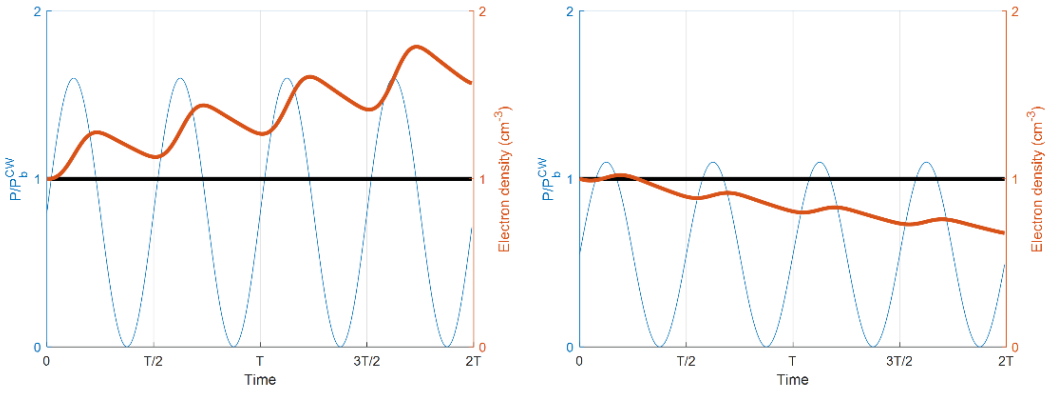

(a) (b)

Fig. 5.1. Change in electron density showing steady (a) growth and (b) fall in the density

Fig. 5.2 shows the similar information within four cycles of the carrier frequency of the signal produced by OOPD1 code. In Fig. 5.2(a), it can be seen that the peak power is high enough for the electron population to steadily grow. In Fig. 5.2(b), the peak power is not high enough, so the number of electrons steadily falls. The results in Fig. 5.2 are in good agreement with those in Fig. 5.1.

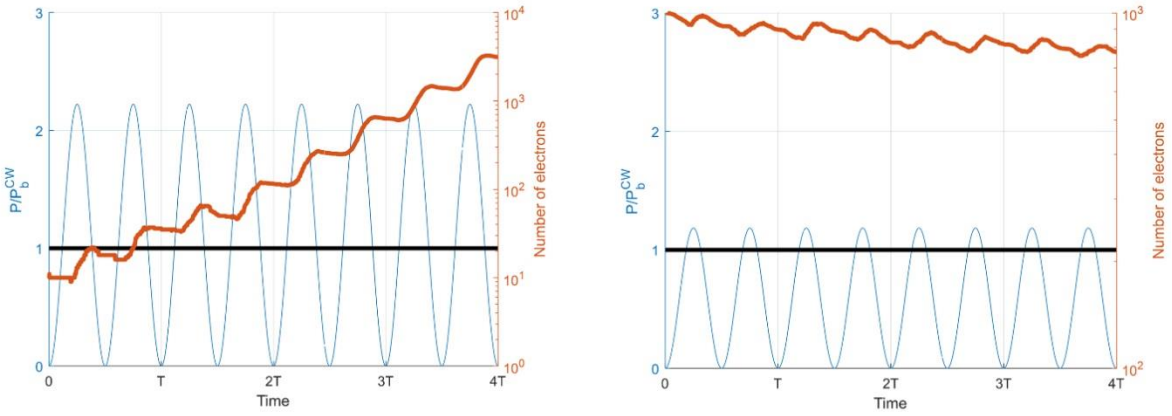

Fig. 5.2. PIC/MCC simulation results of the change in electron density showing steady (a) growth and (b) fall in electron density

Next, the effect of duration of the burst on the growth of electron density is analysed. For a given peak power resulting in a steady growth of electron density, breakdown depends on how long the burst is. For example, breakdown will eventually occur if the waveform in Fig. 5.1(a) is long enough. Fig. 5.3 shows the electron density increase factor as a function of time for different values of normalized peak power P_p/P_b^{CW}. In the simulations of breakdown, only the growth factor in electron density is important. As a result, the initial electron density was set arbitrarily. The source of initial free electrons is from cosmic rays. Previous numerical studies have considered a factor of 10^8 growth (dashed line in Fig. 5.3) from the initial electron density at the start of the simulation as the critical value for electrical breakdown to occur [68, 69]. For example, when $P_p/P_b^{CW} = 2.1$, electrical breakdown will occur if the burst duration is longer than, or equal to, 200 ns which is equivalent to 133 cycles of the carrier frequency ($133T$). If the burst duration is only 144 ns ($<111T$), there are inadequate RF cycles above P_b^{CW}. The peak power needs to increase for the breakdown to occur. In Fig. 5.3, P_p/P_b^{CW} increases to 2.2. Since varying the burst duration affects the electron density, electrical breakdown depends on the duration of a pulse.

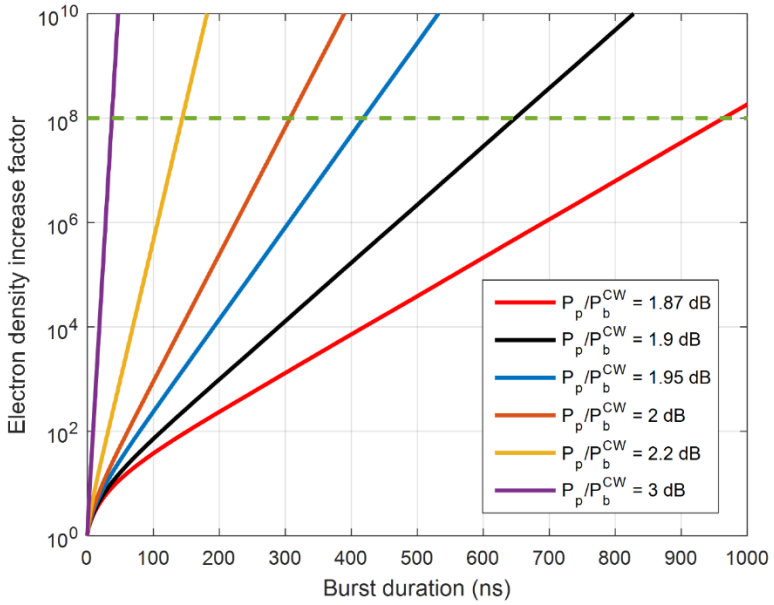

(a)

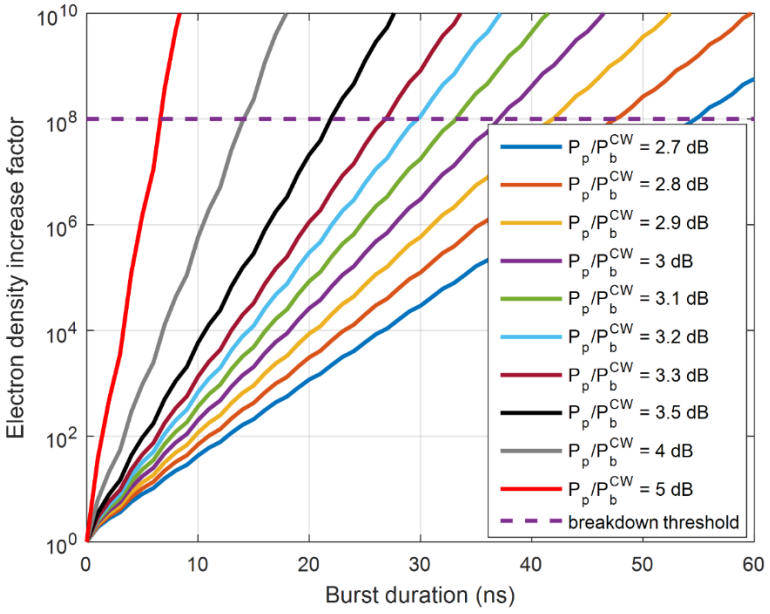

(b)

Fig. 5.3. Required burst duration to breakdown for different peak powers

There is an alternative way to represent the information in Fig. 5.3. Fig. 5.4 shows the normalized peak power P_p/P_b^{CW} as a function of time to breakdown. The time to breakdown is the required duration of the burst for breakdown to occur. In Fig. 5.4, it can be seen that when the time to breakdown increases, P_p/P_b^{CW} decreases. The curve shown in the figure can be referred to as the threshold for breakdown. For example, for a given P_b^{CW}, breakdown will not

take place if the burst is under this curve. However, if the burst is above the curve, breakdown will eventually occur.

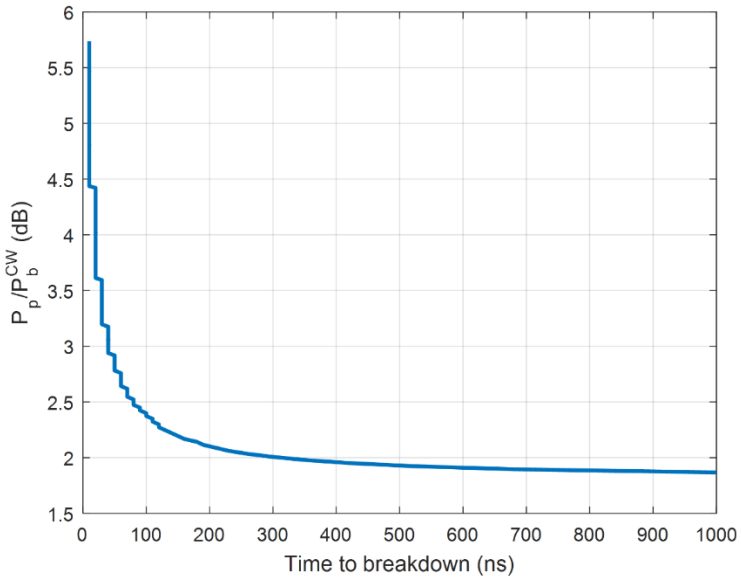

Fig. 5.4. Breakdown curve based on the normalized peak power and the duration of the burst

There are a number of important aspects of Fig. 5.3 and 5.4 which help explain the breakdown results found by RFS. The first is that the lengths of the bursts are of the same order as the elementary periods for DVB which range from 109 ns to 175 ns depending on the DVB bandwidth. This suggests that breakdown depends on the very short term properties of the OFDM signal and probably depends on only one, or at most a few adjacent values of the time-domain vector $\boldsymbol{x} = [x_0\ x_1\ x_2\ \ldots\ x_{N-1}]^T$. Another aspect is the form of the curve. For bursts less than 100 ns, the value of P_p/P_b^{CW} increases very rapidly, whereas for bursts between 100 and 400 ns P_p/P_b^{CW} changes by only a fraction of a dB. Finally, it suggests that breakdown will occur at lower powers for lower bandwidth DVB systems which have longer elementary periods.

These results cannot be directly applied to an OFDM signal as the peaks are in general not bursts of sinusoids of constant amplitude, unless perhaps the peaks are severely clipped.

5.3 Properties of peaks in DVB-T signals

In this section, the statistics of the heights and widths of signal peaks in relation to electrical breakdown are studied. These studies are then used to explain results of the RFS experiments.

Future mitigation techniques for reducing the likelihood of electrical breakdown are also discussed.

5.3.1 Statistics of the heights and widths of signal peaks

There is little in the literature on the distribution of pulse width because it is not important in most OFDM applications. Therefore, this is one of the few studies of pulse width of OFDM. The distribution of pulse width of OFDM is simulated. In the simulation, 4-QAM constellation was used and 1 million symbols were simulated. The signal has N = 2048 subcarriers in the 2K mode where 1705 subcarriers are used, and 343 subcarriers are unused. The signal is undistorted, so high PAPR is possible, however, with a low probability of occurrence.

Fig. 5.5 shows how the form of a typical peak and how the width of a pulse is calculated. The calculation level to average power ratio (CLAPR) is used to identify the power level at which the pulse width is calculated with reference to the average power level. The peak is narrowest at the top and broadens as the CLAPR decreases. In the simulation, the baseband signal with oversampling factor of 8 was used. Fig. 5.6 shows the pulse width distribution of the DVB-T signal. The probability on the vertical axis is the ratio of the number of pulses having a certain width to the number of elementary time periods simulated. The results can be applied to any of the DVB-T bandwidths simply by substituting the appropriate value of T_E.

It can be seen that as the CLAPR increases from 9 dB to 14 dB the probability decreases rapidly. In other words, very high peaks happen much less frequently than smaller peaks. For CLAPR of 9 dB, the most common pulse width is around $0.5T_E$ and this occurs with a probability of around 5×10^{-4}. When the CLAPR increases to 14 dB, the most common pulse width reduces to around $0.3T_E$ and this occurs with a probability of around 10^{-9}. To put this in context, for the 8 MHz standard a pulse with CLAPR of 14 dB will occur on average around every 109 seconds while one with a CLAPR of 9 dB will occur around every 0.2 milliseconds.

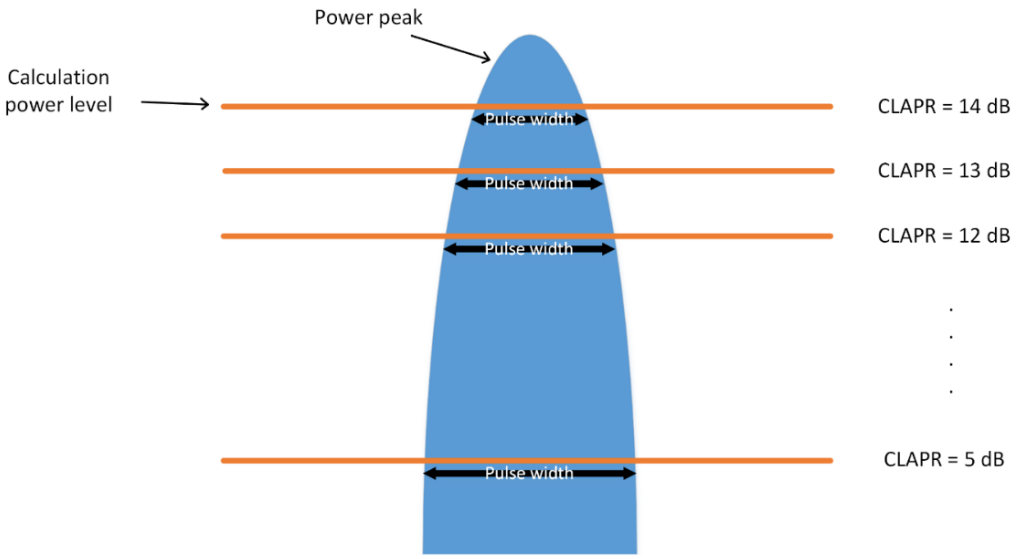

Fig. 5.5. A diagram showing how the pulse width is calculated with reference to average power of the signal

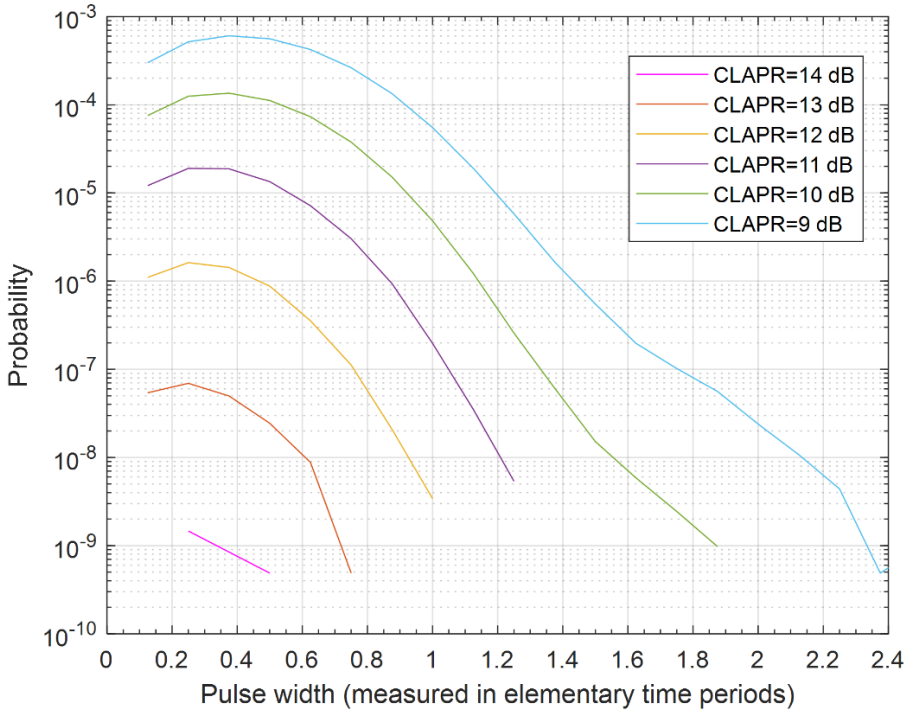

Fig. 5.6. Distribution of pulse width of a DVB-T signal

5.3.2 Explanation of RFS experimental results

While the results above cannot explain the precise details of the results found in the RFS experiment they can be used to justify the general form of the graphs and the fact that it is the

average power of the OFDM signal rather than the peak power which follows the expected form of the Paschen curve.

Fig. 5.7 shows typical waveforms for an undistorted OFDM peak (Fig 5.7(a)) and one which is hard clipped (Fig 5.7(b)). The hard clipped pulse can reasonably be approximated by a burst of sinusoidal signal of length given by the pulse width at that level, while the unclipped pulse only has the peak value for a short time. This means that a much higher peak will be required to cause breakdown for the unclipped signal. Thus, the difference of ~5 dB between the results for short pulses and long pulses in Fig. 5.6 (equivalent to 5 dB reduction in P_p in Fig 5.7(b)) provides an explanation of the variation of ~5 dB shown in Fig 2.9.

To understand the relationship in greater depth, would require more experiments and more detailed information about the properties of the DVB-T test transmitter. In particular, is the pressure at each power level reduced sufficiently slowly to allow the system to reach steady state and breakdown to occur only for the low probability high peaks? Also, in what way precisely are the peak values limited as the power level is increased? Finally, are the random data sequences generated by the transmitter sufficiently long to ensure low probability peaks will occur?

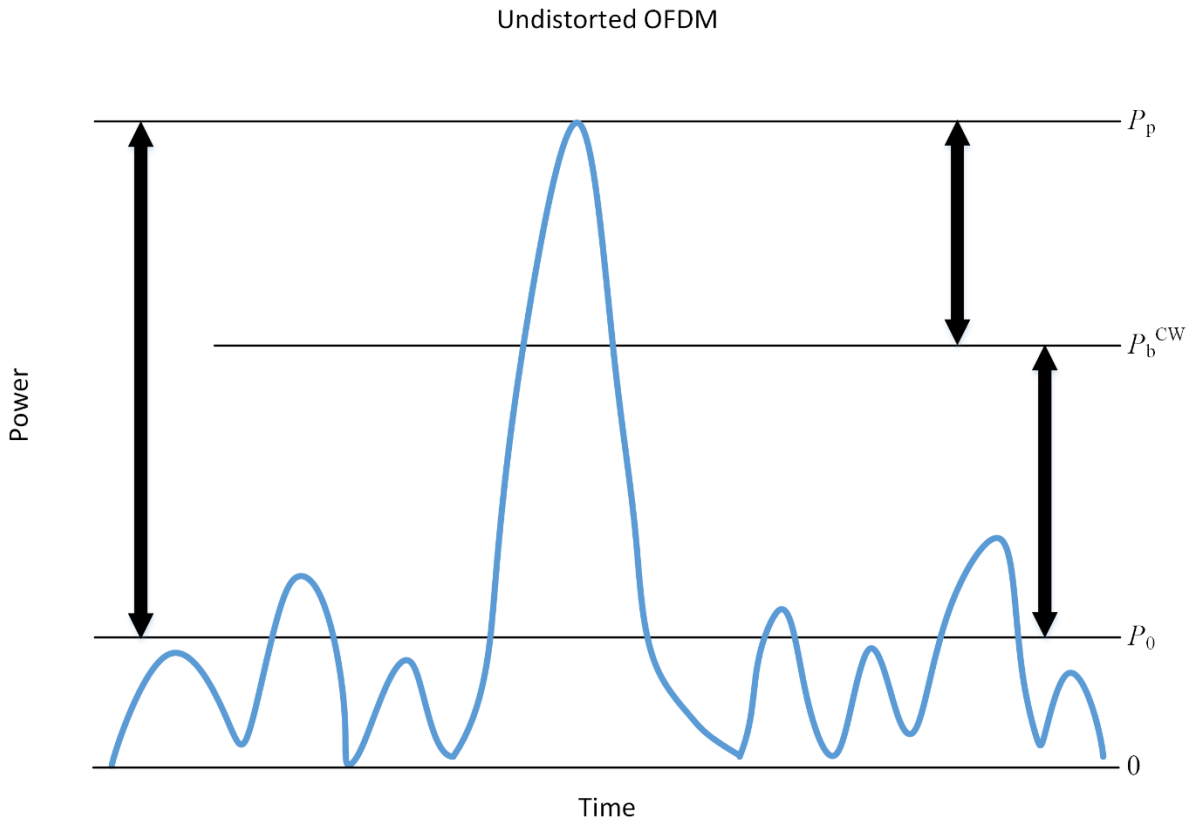

(a)

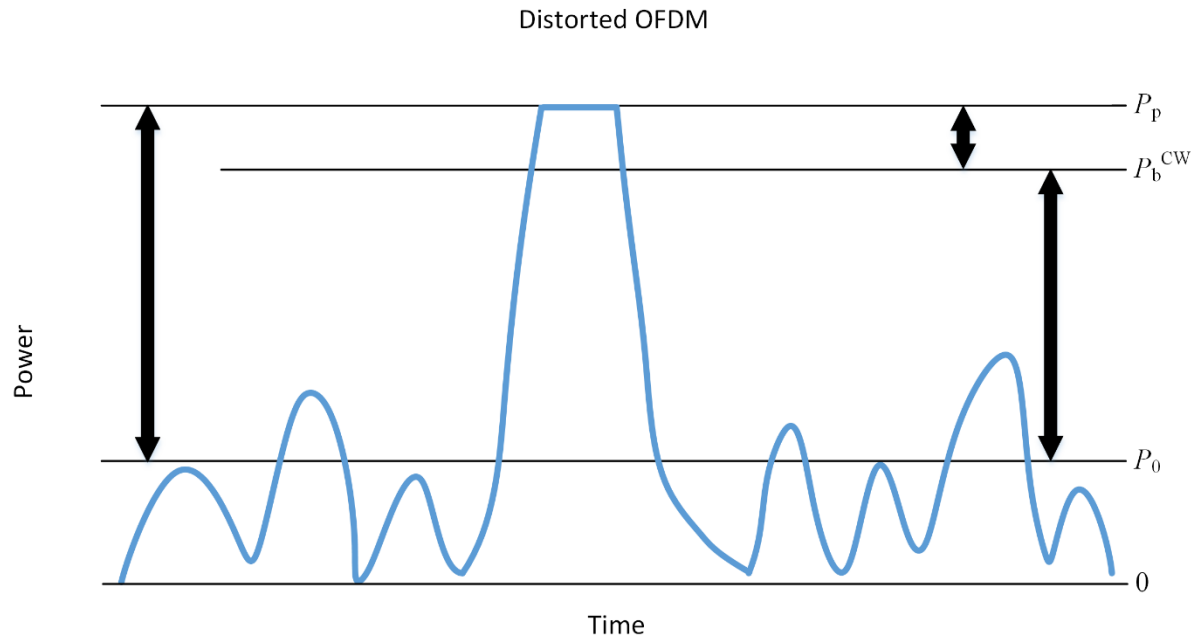

(b)

Fig. 5.7. Pulse shapes for an (a) undistorted OFDM peak and (b) a clipped peak

5.3.3 Future mitigation techniques

An interesting area of future research would be the development of techniques which modify the OFDM signal in ways that reduce the probability of breakdown for a given average power but do not affect the overall bit error rate performance. The results in the previous sections show that breakdown is likely to result from high peaks which have widths of the order of the elementary period T_E . The size and shape of these peaks depend very strongly on only one or two adjacent baseband samples. Peaks which are both high and wide are most likely to be the result of two adjacent high samples. Fig. 5.8 shows the pulse shape that results from two high amplitude baseband samples which are preceded and followed by two very low samples. It shows that the peak of the signal depends on the relative phase of the two samples, with the height of the peak decreasing as the phase difference increases.

New digital signal processing algorithms may be possible which identify baseband sequences which will lead to very high peaks and reducing the two samples. As high peaks occur so rarely, this would have negligible effect on the bit error rate or out of band power of the system.

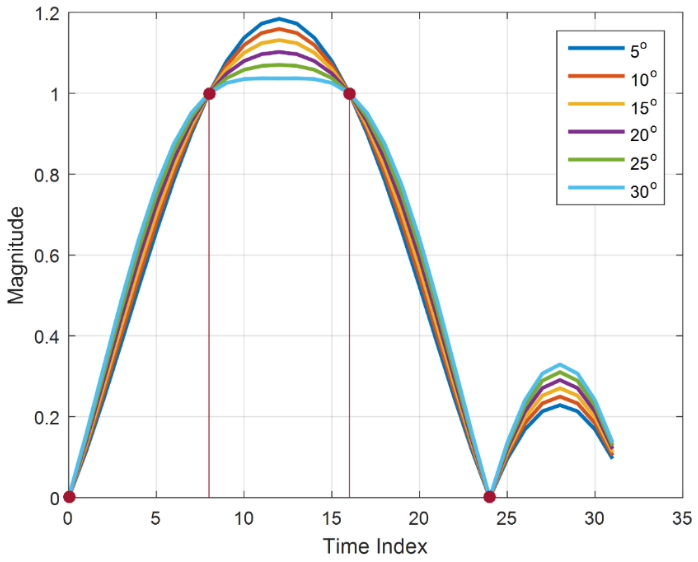

Fig. 5.8. Resulting magnitude of oversampled signal as the phase difference between x_1 and x_2 varies

5.4 The Effect of Carrier Frequency

The effect of the carrier frequency of a DVB-T signal on electrical breakdown is investigated. In OFDM modulation systems, a baseband signal is up-converted to transmit over through an RF channel. For 6 MHz UHF channels, the carrier frequency (MHz) of a DVB-T signal has been given by [1]

$$f_c = 470 + 6(\mathrm{k} + 0.5), \quad k = 0, 1, 2, 3, \ldots \tag{5.1}$$

The electron density resulted from a DVB-T signal with a carrier frequency of 473 MHz and 803 MHz respectively is calculated. To compare the performance the simulations used in Fig. 5.3 were repeated for 473 MHz and 803 MHz.

Fig. 5.9(a) and (b) show the similar information in Fig. 5.3 for the carrier frequency of 473 MHz and 803 MHz respectively. It can be seen that change in the burst duration for the different frequencies is negligible. Thus, the carrier frequency of the signal has no significant effect on electrical breakdown.

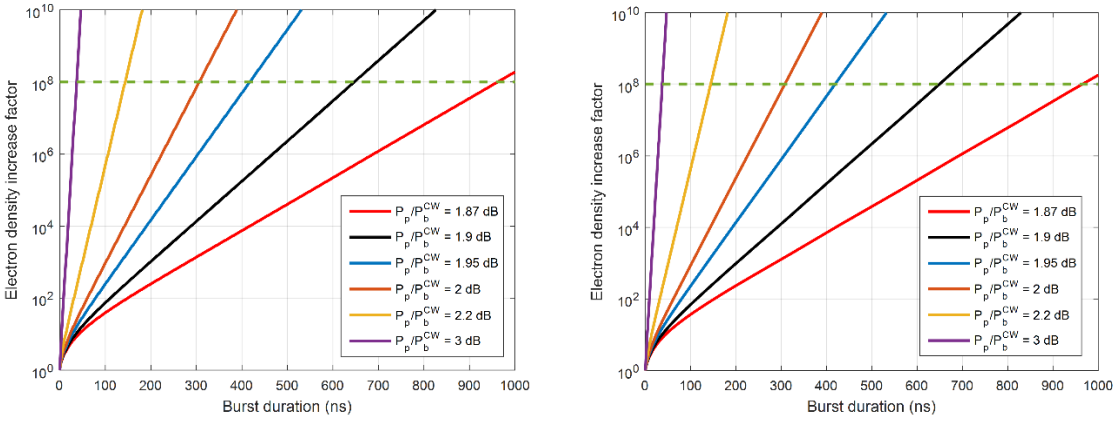

(a) (b)

Fig. 5.9. Required burst duration to breakdown for the carrier frequency of (a) 473 MHz and (b) 803 MHz

5.5 Conclusions

In this chapter the effect of signal waveform on the growth of electron density has been investigated. Results have been presented showing the length of sinusoidal burst of given power required to cause breakdown. These show that high power bursts of length of the order of the elementary period of a DVB-T signal can cause breakdown. Simulations were performed to determine the distributions of the widths of large peaks of a given height for European standard DVB-T signals. It was shown that these high peaks also have lengths of the order of the elementary period of a DVB-T signal. A combination of these two findings were then used to explain results of the RFS experiments. It was shown that the channel bandwidth influences the breakdown behaviour as the electron density increases when the bandwidth decreases. It has also been found that the carrier frequency of the signal has negligible effect on electrical breakdown as the change in electron density for different carrier frequencies over the TV frequency bands is insignificant. The possibility of new digital signal processing algorithms which can identify baseband sequences which will lead to very high peaks was suggested.

Chapter 6: Conclusion

In this thesis, electrical breakdown influenced by the statistics of OFDM signals has been studied. Breakdown occurs when there is enough density of free electrons in the air cavity to create a conductive path between the electrodes. As such, the relationship between the electron density and the time-varying electric field caused by OFDM signals has been investigated. The ionization kinetics equation has been used to calculate the change in electron density in a fixed volume of air. The equation has been applied to bursts of sinusoidal signals and it has been shown that whether breakdown occurs depends on the power and duration of the burst. These results predict that breakdown depends on the short term statistics of the DVB-T signal. Simulation results for the statistical properties of DVB-T signals have been presented which show that there is a very strong relationship between the power and the width of peaks in the signal. It has been shown that these two findings can be combined to explain the previously unexplained results of the high power filter breakdown experiments. Possible new types of digital signal processing algorithms have been discussed which modify the transmitted signal so that peaks that will cause breakdown are removed. It has also been shown that the carrier frequency of the signal has negligible effect on electrical breakdown.

References

[1] I. European Telecommunications Standards, "Digital Video Broadcasting (DVB); Framing structure, channel coding and modulation for digital terrestrial television," 2009.

[2] J. Armstrong, "OFDM for Optical Communications," *Journal of Lightwave Technology,* vol. 27, no. 3, pp. 189-204, 2009.

[3] R. J. Cameron, *Microwave filters for communication systems : fundamentals, design, and applications*. Wiley-Interscience, 2007.

[4] Rohde&Schwarz. (2011). *R&S®SCx8000 Family of UHF/VHF Transmitters - Data sheet (V 04.01 ed.)*.

[5] H. Seung Hee and L. Jae Hong, "An overview of peak-to-average power ratio reduction techniques for multicarrier transmission," *IEEE Wireless Communications,* vol. 12, no. 2, pp. 56-65, 2005.

[6] T. Jiang and Y. Wu, "An Overview: Peak-to-Average Power Ratio Reduction Techniques for OFDM Signals," *IEEE Transactions on Broadcasting,* vol. 54, no. 2, pp. 257-268, 2008.

[7] A. E. Jones, T. A. Wilkinson, and S. K. Barton, "Block coding scheme for reduction of peak to mean envelope power ratio of multicarrier transmission schemes," *Electronics Letters,* vol. 30, no. 25, pp. 2098-2099, 1994.

[8] R. W. Bauml, R. F. H. Fischer, and J. B. Huber, "Reducing the peak-to-average power ratio of multicarrier modulation by selected mapping," *Electronics Letters,* vol. 32, no. 22, pp. 2056-2057, 1996.

[9] A. D. S. Jayalath and C. Tellambura, "Reducing the peak-to-average power ratio of orthogonal frequency division multiplexing signal through bit or symbol interleaving," *Electronics Letters,* vol. 36, no. 13, pp. 1161-1163, 2000.

[10] H. Seung Hee and L. Jae Hong, "PAPR reduction of OFDM signals using a reduced complexity PTS technique," *IEEE Signal Processing Letters,* vol. 11, no. 11, pp. 887-890, 2004.

[11] B. S. Krongold and D. L. Jones, "An active-set approach for OFDM PAR reduction via tone reservation," *IEEE Transactions on Signal Processing,* vol. 52, no. 2, pp. 495-509, 2004.

[12] B. Li, W. Xu, H. Zhang, C. Zhao, and L. Hanzo, "PAPR Reduction for Hybrid ACO-OFDM Aided IM/DD Optical Wireless Vehicular Communications," *IEEE Transactions on Vehicular Technology,* vol. 66, no. 10, pp. 9561-9566, 2017.

[13] J. Armstrong, "New OFDM peak-to-average power reduction scheme," in *IEEE VTS 53rd Vehicular Technology Conference, Spring 2001. Proceedings (Cat. No.01CH37202)*, 2001, vol. 1, pp. 756-760 vol.1.

[14] J. Armstrong, "Peak-to-average power reduction for OFDM by repeated clipping and frequency domain filtering," *Electronics Letters,* Article vol. 38, no. 5, pp. 246-247, 2002.

[15] D. Anderson, U. Jordon, M. Lisak, T. Olsson, and M. Ahlander, "Microwave breakdown in resonators and filters," *IEEE Transactions on Microwave Theory and Techniques,* vol. 47, no. 12, pp. 2547-2556, 1999.

[16] D. Anderson, M. Lisak, and T. Lewin, "Breakdown in air-filled microwave waveguides during pulsed operation," *Journal of Applied Physics,* vol. 56, no. 5, pp. 1414-1419, 1984.

[17] K. Frigui *et al.*, "Microwave breakdown in waveguide filters, numerical simulation, and comparison to experiments," *Journal of Applied Physics,* vol. 107, no. 4, p. 043301, 2010.

[18] I. Korolov, A. Derzsi, and Z. Donkó, "Experimental and kinetic simulation studies of radio-frequency and direct-current breakdown in synthetic air," *Journal of Physics D: Applied Physics,* vol. 47, no. 47, p. 475202, 2014.

[19] Y. Sakiyama and D. B. Graves, "Nonthermal atmospheric rf plasma in one-dimensional spherical coordinates: Asymmetric sheath structure and the discharge mechanism," *Journal of Applied Physics,* vol. 101, no. 7, p. 073306, 2007.

[20] S. Anza *et al.*, "Prediction of Multipactor Breakdown for Multicarrier Applications: The Quasi-Stationary Method," *IEEE Transactions on Microwave Theory and Techniques,* vol. 60, no. 7, pp. 2093-2105, 2012.

[21] S. Anza, C. Vicente, D. Raboso, J. Gil, B. Gimeno, and V. E. Boria, "Enhanced prediction of multipaction breakdown in passive waveguide components including space charge effects," in *2008 IEEE MTT-S International Microwave Symposium Digest*, 2008, pp. 1095-1098.

[22] Z. L. Petrović *et al.*, "Measurement and interpretation of swarm parameters and their application in plasma modelling," *Journal of Physics D: Applied Physics,* vol. 42, no. 19, p. 194002, 2009.

[23] B. Chaudhury, J.-P. Boeuf, and G. Q. Zhu, "Pattern formation and propagation during microwave breakdown," *Physics of Plasmas,* vol. 17, no. 12, p. 123505, 2010.

[24] J. Rasch, V. E. Semenov, D. Anderson, M. Lisak, and J. Puech, "On the microwave breakdown stability of a spherical hot spot in air," *Journal of Physics D: Applied Physics,* vol. 43, no. 32, p. 325204, 2010.

[25] K. Frigui *et al.*, "A solution to relax breakdown threshold in waveguide filters," in *Microwave Conference (EuMC), 2012 42nd European*, 2012, pp. 1107-1110.

[26] K. Frigui *et al.*, "Modeling and characterization of microwave breakdown at atmospheric pressure in OMUX filters," *International Journal of RF and Microwave Computer-Aided Engineering,* vol. 24, no. 1, pp. 46-54, 2014.

[27] C. Qian, D. Ding, Z. Fan, and R. Chen, "A fluid model simulation of a simplified plasma limiter based on spectral-element time-domain method," *Physics of Plasmas,* vol. 22, no. 3, p. 032111, 2015.

[28] D. González-Iglesias, M. Ó, B. G. Martínez, M. E. Díaz, V. E. Boria, and P. M. Iglesias, "Multipactor RF Breakdown in Coaxial Transmission Lines With Digitally Modulated Signals," *IEEE Transactions on Electron Devices,* vol. 63, no. 10, pp. 4096-4103, 2016.

[29] S. Saeedi, J. Lee, and H. Sigmarsson, "Prediction of power handling in tunable, high-Q, substrate-integrated, evanescent-mode cavity bandpass filters," *Electronics Letters,* vol. 52, no. 10, pp. 846-848, 2016.

[30] C. Qian, D. Ding, J. Bi, and R. Chen, "Numerical Analysis of Multi-Carrier Microwave Breakdown in Waveguide Components," *IEEE Microwave and Wireless Components Letters,* vol. 26, no. 2, pp. 77-79, 2016.

[31] U. Jordan, V. E. Semenov, D. Anderson, M. Lisak, and T. Olsson, "Microwave breakdown in air for multi-carrier, modulated or stochastically time varying RF fields," *Journal of Physics D: Applied Physics,* vol. 36, no. 7, p. 861, 2003.

[32] H. C. Kim and J. P. Verboncoeur, "Transition of window breakdown from vacuum multipactor discharge to rf plasma," *Physics of Plasmas,* vol. 13, no. 12, p. 123506, 2006.

[33] T. Olsson, D. Andersson, J. Jordan, M. Lisak, V. Semenov, and M. Ahlander, "Microwave breakdown in air-filled resonators," in *Microwave Symposium Digest, 1999 IEEE MTT-S International*, 1999, vol. 3, pp. 915-918 vol.3.

[34] A. Semnani, K. Chen, and D. Peroulis, "Microwave Gas Breakdown in Tunable Evanescent-Mode Cavity Resonators," *IEEE Microwave and Wireless Components Letters,* vol. 24, no. 5, pp. 351-353, 2014.

[35] K. Chen, A. Semnani, and D. Peroulis, "High-power microwave gas discharge in high-Q evanescent-mode cavity resonators and its instantaneous/long-term effects," in *Microwave Symposium Digest (IMS), 2013 IEEE MTT-S International*, 2013, pp. 1-4.

[36] L. Settaouti and A. Settaouti, "Monte Carlo simulation of radio-frequency plasmas in N2," *International Journal of Numerical Modelling: Electronic Networks, Devices and Fields*, vol. 24, no. 2, pp. 99-110, 2011.

[37] A. SETTAOUTI and L. SETTAOUTI, "SIMULATION OF ELECTRON SWARM PARAMETERS IN AIR," *International Journal of Modern Physics B*, vol. 20, no. 10, pp. 1233-1242, 2006.

[38] H. B. Smith, C. Charles, and R. W. Boswell, "Breakdown behavior in radio-frequency argon discharges," *Physics of Plasmas*, vol. 10, no. 3, p. 875, 2003.

[39] A. Semnani, A. Venkattraman, A. A. Alexeenko, and D. Peroulis, "Frequency response of atmospheric pressure gas breakdown in micro/nanogaps," *Applied Physics Letters*, vol. 103, no. 6, p. 063102, 2013.

[40] B. Grycz, *FOURTH STATE OF MATTER*.

[41] M. Yu, "Power-handling capability for RF filters," *IEEE Microwave Magazine*, vol. 8, no. 5, pp. 88-97, 2007.

[42] M. Savic, M. Radmilovic-Radjenovic, M. Suvakov, S. Marjanovic, D. Maric, and Z. L. Petrovic, "On Explanation of the Double-Valued Paschen-Like Curve for RF Breakdown in Argon," *IEEE Transactions on Plasma Science*, vol. 39, no. 11, pp. 2556-2557, 2011.

[43] V. A. Lisovskii, "Criterion for microwave breakdown of gases," *Technical Physics*, journal article vol. 44, no. 11, pp. 1282-1285, 1999.

[44] R. P. Richard van. Nee, *OFDM for wireless multimedia communications*. Boston : Artech House 2000

[45] T. Jiang, M. Guizani, H. Chen, W. Xiang, and Y. Wu, "Derivation of PAPR Distribution for OFDM Wireless Systems Based on Extreme Value Theory," *IEEE Transactions on Wireless Communications*, vol. 7, no. 4, pp. 1298-1305, 2008.

[46] C. K. Birdsall, "Particle-in-cell charged-particle simulations, plus Monte Carlo collisions with neutral atoms, PIC-MCC," *IEEE Transactions on Plasma Science*, vol. 19, no. 2, pp. 65-85, 1991.

[47] V. Vahedi, G. DiPeso, C. K. Birdsall, M. A. Lieberman, and T. D. Rognlien, "Capacitive RF discharges modelled by particle-in-cell Monte Carlo simulation. I.

Analysis of numerical techniques," *Plasma Sources Science and Technology*, vol. 2, no. 4, p. 261, 1993.

[48] V. Vahedi, C. K. Birdsall, M. A. Lieberman, G. DiPeso, and T. D. Ronhlien, "Capacitive RF discharges modelled by particle-in-cell Monte Carlo simulation. II. Comparisons with laboratory measurements of electron energy distribution functions," *Plasma Sources Science and Technology*, vol. 2, no. 4, p. 273, 1993.

[49] L. E. Kline and J. G. Siambis, "Computer Simulation of Electrical Breakdown in Gases; Avalanche and Streamer Formation," *Physical Review A*, vol. 5, no. 2, pp. 794-805, 1972.

[50] T. Itoh and T. Musha, "Monte Carlo Calculations of the Motions of Electrons in Helium," *Journal of Applied Physics*, vol. 31, no. 4, p. 744, 1960.

[51] M. J. Kushner, "Monte-Carlo simulation of electron properties in rf parallel plate capacitively coupled discharges," *Journal of Applied Physics*, Article vol. 54, no. 9, pp. 4958-4965, 1983.

[52] M. J. Kushner, H. N. Anderson, and P. J. Hargis, "Simulation of Spatially Dependent Excitation Rates and Power Deposition in RF Discharges for Plasma Processing," *MRS Proceedings*, vol. 38, p. 201, 2011, Art. no. 201.

[53] L. E. Kline, W. D. Partlow, and W. E. Bies, "Electron and chemical kinetics in methane rf glow-discharge deposition plasmas," *Journal of Applied Physics*, vol. 65, no. 1, p. 70, 1989.

[54] S. Dujko, Z. M. Raspopović, and Z. L. Petrović, "Monte Carlo studies of electron transport in crossed electric and magnetic fields in CF4," *Journal of Physics D: Applied Physics*, vol. 38, no. 16, pp. 2952-2966, 2005.

[55] Y. P. Raizer, *Gas discharge physics*. Berlin ; New York : Springer 1997

[56] V. Vahedi and M. Surendra, "A Monte Carlo collision model for the particle-in-cell method: applications to argon and oxygen discharges," *Computer Physics Communications*, vol. 87, no. 1, pp. 179-198, 1995/05/02 1995.

[57] H. B. Smith, C. Charles, R. W. Boswell, and H. Kuwahara, "Bias formation in a pulsed radiofrequency argon discharge," *Journal of Applied Physics*, Article vol. 82, no. 2, pp. 561-565, 1997.

[58] E. Kawamura, C. K. Birdsall, and V. Vahedi, "Physical and numerical methods of speeding up particle codes and paralleling as applied to RF discharges," *Plasma Sources Science and Technology*, vol. 9, no. 3, p. 413, 2000.

[59] P. Diomede, M. Capitelli, and S. Longo, "Effect of discharge voltage on capacitively coupled, parallel plate rf hydrogen plasmas," *Plasma Sources Science and Technology,* vol. 14, no. 3, pp. 459-466, 2005.

[60] S. Longo, "Monte Carlo simulation of charged species kinetics in weakly ionized gases," *Plasma Sources Science and Technology,* vol. 15, no. 4, pp. S181-S188, 2006.

[61] A. Settaouti and L. Settaouti, "Monte Carlo simulation of electrical corona discharge in air," *Electric Power Systems Research,* vol. 81, no. 1, pp. 84-89, 2011.

[62] P. T. a. S. G. PLASMA DEVICE SIMULATION CODES, EECS Department, University of California, Berkeley.

[63] J. T. Gudmundsson, E. Kawamura, and M. A. Lieberman, "A benchmark study of a capacitively coupled oxygen discharge of the oopd1 particle-in-cell Monte Carlo code," *Plasma Sources Science and Technology,* vol. 22, no. 3, p. 035011, 2013.

[64] W. C. Taylor, W. E. Scharfman, and T. Morita, "Voltage Breakdown of Microwave Antennas," in *Advances in Microwaves,* vol. 7, L. E. O. Young, Ed.: Elsevier, 1971, pp. 59-130.

[65] L. Gould and L. W. Roberts, "Breakdown of Air at Microwave Frequencies," *Journal of Applied Physics,* vol. 27, no. 10, pp. 1162-1170, 1956.

[66] P. E. Bisbing, McMenamin, D. L., Jordan, A. K., and Scherer, P. M., "Study to Obtain Design Data for Reentry ECM Antenna Systems," *GE Rep. No. 68SD591. General Electric Co., Philadelphia, Pennsylvania,* 1968.

[67] W. Woo and J. S. DeGroot, "Microwave absorption and plasma heating due to microwave breakdown in the atmosphere," *The Physics of Fluids,* vol. 27, no. 2, pp. 475-487, 1984.

[68] S. K. Nam and J. P. Verboncoeur, "Global model for high power microwave breakdown at high pressure in air," *Computer Physics Communications,* vol. 180, no. 4, pp. 628-635, 2009/04/01/ 2009.

[69] J. P. Booth, G. Cunge, N. Sadeghi, and R. W. Boswell, "The transition from symmetric to asymmetric discharges in pulsed 13.56 MHz capacitively coupled plasmas," *Journal of Applied Physics,* Article vol. 82, no. 2, pp. 552-560, 1997.